Wake interaction of dual surging FOWT rotors in tandem
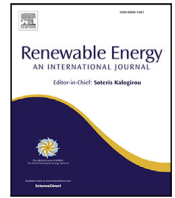
Li, Yuan Tso; Yu, Wei; Sarlak, Hamid

Important note
To cite this publication, please use the final published version (if applicable).
Please check the document version above.

Wake interaction of dual surging FOWT rotors in tandem

YuanTso Li [a,b], Wei Yu [b], Hamid Sarlak [a,*]

[a] *Department of Wind and Energy Systems, Technical University of Denmark, Kgs. Lyngby, 2800, Denmark*
[b] *Faculty of Aerospace Engineering, Delft University of Technology, Delft, 2628 CD, The Netherlands*

ARTICLE INFO

ABSTRACT

To investigate the wake interaction between floating offshore wind turbines (FOWTs), this work presents large eddy simulations of two full-scale surging FOWT rotors in tandem. Rotors are modeled using actuator line technique with the possibility of prescribing surge degree-of-freedom. The study examines two main aspects: the different configurations of fixed and surging rotors, and the phase differences of surging motions when both upstream and downstream rotors are surging. Throughout the simulations, different spacings between the two rotors and different inflow conditions (laminar/turbulent) are explored, leading to a large database of highly resolved simulations. The analysis of different fixed–surging configurations suggests that surging motions are generally beneficial to the system's power output (up to 2% at realistic turbulence intensities) compared to the fixed configuration. The power output increase is claimed to be associated with the surging motion itself and the faster wake recovery. Moreover, we discover that the phase differences of the surging motions have subtle effects on the rotor performance of the downstream rotor, especially for the cases with larger spacing between the two surging FOWTs. As an outcome, the relative difference between the power outputs are smaller than 0.4% when the rotor spacing is five rotor diameters. With the aim that this area can be further explored, selected animations, benchmark data, and the numerical solver developed during this study have been made publicly available through this article.

1. Introduction

To unlock the offshore wind potential at sites with water depths deeper than 60 m, floating offshore wind turbines (FOWTs) are considered more favorable than their bottom-fixed counterparts [1–3]. On the other hand, aspects such as wake interactions of FOWTs subjected to motions have not yet been thoroughly explored [1,4,5]. Up to the present, several experimental and numerical studies have indicated that the motions of FOWT significantly influenced the power performance and wake aerodynamics of FOWTs [6–8]. Moreover, it has also been reported that the wake structures of the FOWT rotors are affected by their motions [9,10], pointing out that the wake interactions of floating offshore wind farms may significantly differ from the traditional bottom-fixed counterparts.

Understanding the wake interactions of wind turbines is critical as they affect the overall wind farms' annual energy production (AEP), optimal layout of wind farms, and fatigue lifetimes of the turbine components, all of which strongly influence the levelized cost of energy (LCoE) [4,11,12]. Although wake interactions between traditional bottom-fixed wind turbines have been studied for more than four decades [12–15], research on wake interactions between FOWTs has

only started very recently (around 2020), and full understanding of them is still lacking [4].

Several studies have already suggested that wake interactions in floating wind farms differ significantly from those in bottom-fixed installations. However, research on such interactions remains rather limited [4], and high-fidelity models like large eddy simulation (LES) are rarely used due to their computational intensity. For instance, Wise et al. [16] employed the dynamic wake meandering model (DWM) to investigate the wake meandering and fatigue loading of two FOWTs in tandem, while no comparison has been made between the cases of surging and the fixed ones. Rezaeiha et al. [17] focused on comparing the power and thrust of a fixed turbine operating in the wake of a fixed or surging turbine using unsteady RANS coupled with actuator disk model, showing that the power output of the downstream turbine would be slightly higher when operating in the wake of a surging upstream turbine than a fixed upstream one. More recently, Ramos-García et al. [5] applied a vortex solver coupled with the lifting line model to evaluate the effects of motion on wake interactions of FOWTs. Their results indicated that compared to fixed turbines, the power performances of downstream turbines that operated in the wake of surging upstream turbines were significantly increased when

---

* Corresponding author.
  E-mail address: hsar@dtu.dk (H. Sarlak).

under laminar inflow conditions due to faster wake recoveries, but the improvements were drastically diminished when under turbulent inflow conditions. Despite these contributions, the above-mentioned works employed models that have some shortcomings in resolving the transient and turbulence properties of the flow [5,18]. In light of this, to provide additional insight and knowledge about wake interactions between FOWTs, this work uses a high-fidelity CFD setup that is capable of resolving transient properties and fine flow structures, namely large eddy simulation (LES) with actuator line model (ALM), to model the aerodynamic of the two FOWT rotors. In order to keep the analysis focused, the configurations of the FOWTs' layout are limited to two rotors in tandem, and only surging motions are focused, as it directly affects the apparent inflow velocity seen by the rotor [4,19].

The current study continues the work of Li et al. [10], which focuses on the wake systems of a single FOWT rotor. Extending the scope of isolated turbines, a second FOWT rotor is introduced at downstream positions. With the dual-rotor system, wake interactions of FOWTs are analyzed, and the focus is placed on investigating how the upstream FOWT affects the downstream one.

This work investigates two key aspects of the wake interactions between two FOWT rotors in tandem. First, the effects of different fixed–surging configurations (F–S configurations) on the wake interactions of the two rotors are explored in all four possible combinations. That is, cases with both rotors being fixed (fixed–fixed), one rotor being fixed and the other being surging (surging–fixed and fixed–surging), and both rotors being surging (surging–surging) are investigated. Next, the effects of the phase difference between the two surging motions for the two surging rotors ($\Delta_{\phi_{S_0}}$) are examined (see Fig. 1 and Eq. (3) for a visual explanation and the definition of $\Delta_{\phi_{S_0}}$). Moreover, these two aspects are tested with two inflow conditions: laminar and turbulent (TI= 5.3%). Additionally, two inter-spacings between the two rotors ($\Delta_D = 3D$ and $5D$) are tested to gain a comprehensive understanding.

The two aspects mentioned above are critical for studying the wake interactions of FOWTs. First, instead of only considering the cases with both rotors being surging or fixed, cases with different F–S configurations give deeper insights into how each surging motion affects the aerodynamics of the dual-rotor systems. Second, the effects of phase differences ($\Delta_{\phi_{S_0}}$) are not only interesting but also practically important. For a floating offshore wind farm, even when all FOWTs are subjected to identical periodic motions, additional degrees of freedom still exist, which are the values of phase differences between the motions. Thus, understanding the impacts of the phase differences of FOWT motions on the wake interaction can be beneficial in designing upcoming floating offshore wind farms. So far, neither of these aspects has yet been thoroughly studied, especially the latter, which remained unexplored within the CFD community to the best of the authors' knowledge.

2. Methodology

2.1. Wind turbine rotor model

The wind turbine rotor model utilized in the CFD simulations is the three-bladed NREL 5MW baseline turbine [21]. It has a rotor diameter of $D = 126$ m, a rated wind speed of $V_{0,\text{rated}} = 11.4$ m/s, and a tip speed ratio at rated conditions of $\lambda_{\text{rated}} = 7.0$. In this study, the towers of the NREL 5MW are omitted. Besides, the tilt angles, pre-coning, elastic, ground effects, and wind shear are also not considered. These simplifications make the system (close to) axis-symmetric and allow for a more straightforward analysis.

2.2. Surging settings and phase-averaging

For all the surging rotors considered in this article, the surging amplitudes, A_S^{up} and A_S^{down}, and the surging frequencies, ω_S^{up} and ω_S^{down}, are set to 4 m and 0.63 rad/s, respectively (the superscripts indicate whether the parameters are for the upstream or downstream rotors). A_S and ω_S for both the upstream and downstream rotors are set to the same values since they are mainly dominated by hydrodynamic loads [22], which are assumed to be the same for the two FOWTs. The selection of 4 m and 0.63 rad/s are based on the available metocean data [23] and the analysis of previous studies [10,24,25] (for the floating platform being semi-submersible or tension-leg platform, $\omega_S = 0.63$ rad/s meets the typical sea states while $A_S = 4$ m is larger than the typical values but falls in the reasonable range). Moreover, TI =5.3% is focused on the cases subjected to turbulent inflows, as it is common for typical offshore environments [26]. The positions of the rotors in the computational domain is described by p_R^{up} and p_R^{down}, in Eqs. (1) and (2), where $p_{R_0}^{\text{up}}$ and $p_{R_0}^{\text{down}}$ are the neutral positions of the rotors. When both rotors are surging, the phase difference of the surging motions between the two rotors $\Delta_{\phi_{S_0}}$ is defined as Eq. (3). Unless mentioned otherwise, the initial phase shifts for the surging motions ($\phi_{S_0}^{\text{up}}$ and $\phi_{S_0}^{\text{down}}$ in Eqs. (1) and (2)) are both set to 0.0π. Moreover, with the definitions of p_R^{up} and p_R^{down}, the surging velocity of the upstream and downstream rotor (V_S^{up} and V_S^{down}) can be written as Eq. (4).

$$p_R^{\text{up}}(t) = A_S^{\text{up}} \sin\left(\omega_S^{\text{up}} t + \phi_{S_0}^{\text{up}}\right) + p_{R_0}^{\text{up}} = A_S^{\text{up}} \sin \phi_{S_0}^{\text{up}} + p_{R_0}^{\text{up}} \tag{1}$$

$$p_R^{\text{down}}(t) = A_S^{\text{down}} \sin\left(\omega_S^{\text{down}} t + \phi_{S_0}^{\text{down}}\right) + p_{R_0}^{\text{down}} = A_S^{\text{down}} \sin \phi_{S_0}^{\text{down}} + p_{R_0}^{\text{down}} \tag{2}$$

$$\Delta_{\phi_{S_0}} = \phi_{S_0}^{\text{up}} - \phi_{S_0}^{\text{down}} \tag{3}$$

$$V_S^{\text{up}} = A_S^{\text{up}} \omega_S^{\text{up}} \cos \phi_S^{\text{up}}, \qquad V_S^{\text{down}} = A_S^{\text{down}} \omega_S^{\text{down}} \cos \phi_S^{\text{down}} \tag{4}$$

The operational conditions of the upstream rotors are set to match the rated conditions, which means that the freestream velocity V_0 and the rotor rotational frequency Ω^{up} are set to 11.4 m/s and 1.27 rad/s, respectively. As for the downstream rotor, the rotational speed $\Omega^{\text{down}} = 2\Omega^{\text{up}}/3 = 0.84$ rad/s is set. The setting of Ω^{down} is chosen in an attempt to maintain $\lambda^{\text{down}} \simeq \lambda_{\text{rated}} = 7.0$ for the downstream rotor, which is based on the results of Li et al. [10]. In which the mean disk-averaged streamwise velocities $\bar{u}_{\text{Disk}}$ at $x/D = 3$ and 5 were reported to be around 7.6 m/s (which is $2V_{0,\text{rated}}/3$) when the inflow TI was 5.3% (see the line plots of cases 3^* and 4^* in Fig. 3). Additionally, no controllers are implemented, and the collective pitch angles for the two rotors are kept as $0°$.

In this study, phase-averaging is employed to analyze the effects of periodic surging motions on the aerodynamic quantities. The phase-averaging technique was applied not only to the periodic surging motion but also to the rotor's rotational frequency. This was possible because the rotational frequencies $\Omega^{\text{up/down}}$ were set to be integer multiples of the surging frequencies $\omega_S^{\text{up/down}}$. Specifically, $3\Omega^{\text{up/down}}$ divided by $\omega_S^{\text{up/down}}$ is designed to result in integer values. Notice that factor three is attributed to the 120° symmetry of the three-blade rotor. With this relationship, a specific surging phase angle ($\phi_S^{\text{up/down}}$ as described in Eqs. (1) and (2)) will consistently correspond to a specific rotational phase angle ($\phi_{\Omega}^{\text{up/down}}$ in Eq. (5), where the initial phase shifts $\phi_{\Omega_0}^{\text{up/down}}$ are set to 0.0π in this work). Consequently, the effects of asynchrony between Ω and ω_S in this work are eliminated when applying the phase-averaging technique, making the effects of periodic surging motions more isolated and highlighted [10].

When utilizing the phase-averaging technique to examine specific quantities, such as vorticity magnitude $|\omega|$ when $\phi_S = 0\pi$, the data sampled whenever $\phi_S = 0\pi$ are labeled as $|\omega|_{0\pi}$. The quantity $\langle|\omega|\rangle_{0\pi}$, denoting the phase-averaged of $|\omega|$ as $\phi_S = 0\pi$, represents the mean value of $|\omega|_{0\pi}$ over a specified time interval (see Eq. (6)). Similarly,
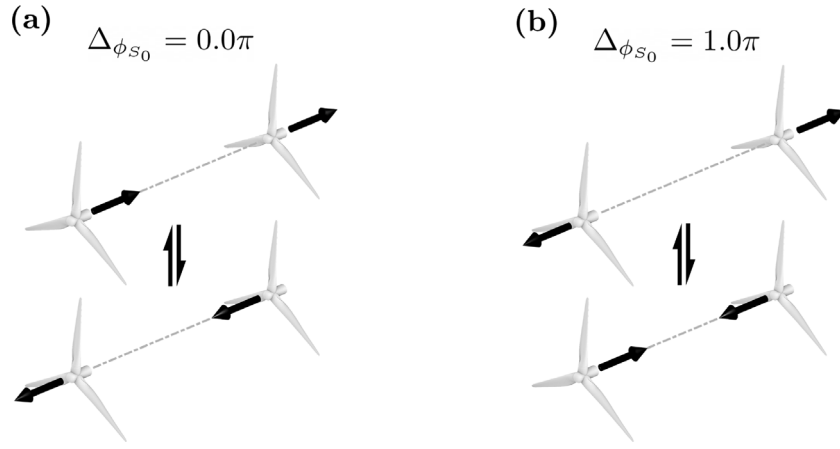
(a) $\Delta_{\phi_{S_0}} = 0.0\pi$

(b) $\Delta_{\phi_{S_0}} = 1.0\pi$

Fig. 1. Schematic diagrams for the phase difference between the two surging motions $\Delta_{\phi_{S_0}}$ (defined in Eq. (3)) of two FOWT rotors in tandem (the CAD model used is a modified DTU 10MW RWT [20]). The surging velocities of the FOWT rotors (V_S^{up} and V_S^{down}) are represented with the black arrows illustrate. (a): The two surging motions with $\Delta_{\phi_{S_0}} = 0.0\pi$ (in-phase, where $V_S^{\text{up}} = V_S^{\text{down}}$). (b): The two surging motions with $\Delta_{\phi_{S_0}} = 1.0\pi$ (out-of-phase, where $V_S^{\text{up}} = -V_S^{\text{down}}$).

$\langle C_P \rangle$ represents the cycle-averaged C_P (averaged C_P based on ϕ_S) over an entire surging cycle (see Fig. 4 for examples). Note that if neither rotor is surging, the sampling rate for phase-averaging related quantities is still set to ω_S, which is 0.63 rad/s (equals to $\Omega^{\text{up}}/2$ and $3\Omega^{\text{down}}/4$). Furthermore, the windows to acquire statistics are 25 complete surging cycles for all the cases, which are deemed sufficient to reach statistical convergence based on the work of Li et al. [10] and Li [27].

$$\phi_\Omega^{\text{up}} = \Omega^{\text{up}}t + \phi_{\Omega_0}^{\text{up}}, \qquad \phi_\Omega^{\text{down}} = \Omega^{\text{down}}t + \phi_{\Omega_0}^{\text{down}} \tag{5}$$

$$\langle|\omega|\rangle_{0\pi} = \frac{\sum_{n=1}^{N} |\omega|_{0\pi,n}}{N} \tag{6}$$

2.3. Simulation frameworks

The CFD simulation cases run in this work use LES for turbulence closure, and they are performed with *OpenFOAM v2106*, an open-source finite-volume-based CFD solver. The flow (air, $\rho = 1.225$ kg/m³ and $\nu = 1.5 \times 10^{-5}$ m²/s) is treated incompressible and Newtonian, and thermal effects are not considered. The governing equations, which are the filtered three-dimensional incompressible Navier–Stokes equations, are written in Eqs. (7) and (8), where u_i is the filtered velocity. The eddy–viscosity model is employed through ν_T in Eq. (8), and the standard Smagorinsky model ($C_k = 0.094$ and $C_\varepsilon = 1.048$) is selected as the subgrid-scale (SGS) model to obtain values of ν_T (Eq. (9)). The spatial and temporal discretization schemes used are the second-order central differencing scheme (`Gauss linear`) and Crank–Nicolson scheme (`CrankNicolson`, with a coefficient of 0.9). PISO (Pressure-Implicit with Splitting of Operators) algorithm is implemented to solve the pressure–velocity system, as Courant–Friedrichs–Lewy numbers are kept well below 1 for the entire domain. High-performance computing clusters of the DTU Computing Center (DCC) [28] serve as the hardware to carry out the simulations. Generally, 600 s simulation time takes around 66 h on 64 processors (Lenovo ThinkSystem SD530 with the processors being Intel Xeon Gold 6126).

$$\frac{\partial u_i}{\partial x_i} = 0 \tag{7}$$

$$\frac{\partial u_i}{\partial t} + u_j \frac{\partial u_i}{\partial x_j} = -\frac{1}{\rho}\frac{\partial p}{\partial x_i} + \frac{\partial}{\partial x_j}\left[(\nu + \nu_T)\left(\frac{\partial u_i}{\partial x_j} + \frac{\partial u_j}{\partial x_i}\right)\right] + \frac{f_{\text{body},i}}{\rho} \tag{8}$$

$$\nu_T = C_k \Delta \sqrt{k_{\text{sgs}}} = C_k\sqrt{\frac{C_k}{C_\varepsilon}}\Delta^2\sqrt{2S_{pq}S_{pq}}, \qquad S_{pq} = \frac{1}{2}\left(\frac{\partial u_p}{\partial x_q} + \frac{\partial u_q}{\partial x_p}\right) \tag{9}$$

The computational domains and grids used for the simulations are shown in Fig. 2. Fig. 2(b) corresponds to the laminar cases with approximately 10.4 M cells, while Fig. 2(c) represents the turbulent cases with around 10.9 M cells. The minor discrepancies are designed to alleviate the unwanted pressure fluctuations generated by the synthetic turbulent inlet conditions (see Li et al. [10] for details). The grids consist of cubic cells generated using `snappyHexMesh`. The "Level" in Fig. 2 refers to the refinement levels, where the grid size Δ doubles as "Level" decreases by one. Δ at "Level" 4, where the rotors are located, is set to $D/80$, making Δ match the spacings between the actuator line point Δ_r. A Cartesian coordinate system with positive x pointing downstream is adopted. The upstream rotor's center is situated at the origin, and the downstream rotor is in tandem in the streamwise direction with the spacing being Δ_D, which is set to be $3D$ or $5D$ when they are in their neutral positions. Both rotors rotate clockwise when viewed from the upstream, and $\phi_\Omega^{\text{up/down}} = 0.0\pi$ corresponds to a blade pointing in the positive z-direction. For temporal resolution, 360 time steps are used for one rotor revolution under its rated conditions ($\Delta t = 0.0138$ s), ensuring the rotors' tips travel less than a single Δ per time step.

The inlet boundary conditions of velocity for the laminar cases apply a fixed uniform value, while the turbulent cases employ a built-in synthetic turbulent inlet method of OpenFOAM v2106, which is divergence-free synthetic eddy method (DFSEM, `turbulentDF-SEMInlet`). DFSEM introduces desired turbulence characteristics (mean velocity, turbulence intensity, and length scale) with lower computational resources compared to precursor methods [29]. The characteristics of turbulence had been sampled and characterized in Li et al. [10], and all the cases with turbulent inflow conditions in this paper have a turbulence intensity of TI= 5.3%, which is deemed typical for offshore environments [26]. It should be noted that ground and wind shear is not imposed for both laminar and turbulent inlet conditions. Apart from the inlets, both the laminar and turbulent cases shared the same boundary conditions for the velocity, which are slip walls for the four sides and advective boundary conditions (D/D$t = 0$) is assigned for the outlet. For pressure p, symmetry boundary conditions are applied for the sides and inlet, while the outlet is set to have a fixed uniform value, assuming the ambient pressure is recovered before the outlet ($x/D = 10$).

2.4. Rotor parameterization

A modified version of `turbinesFoam`, developed by Bachant et al. [30], is used to implement ALM for the surging FOWT rotors, which we called `surgingTurbinesFoam`. ALM parameterizes the
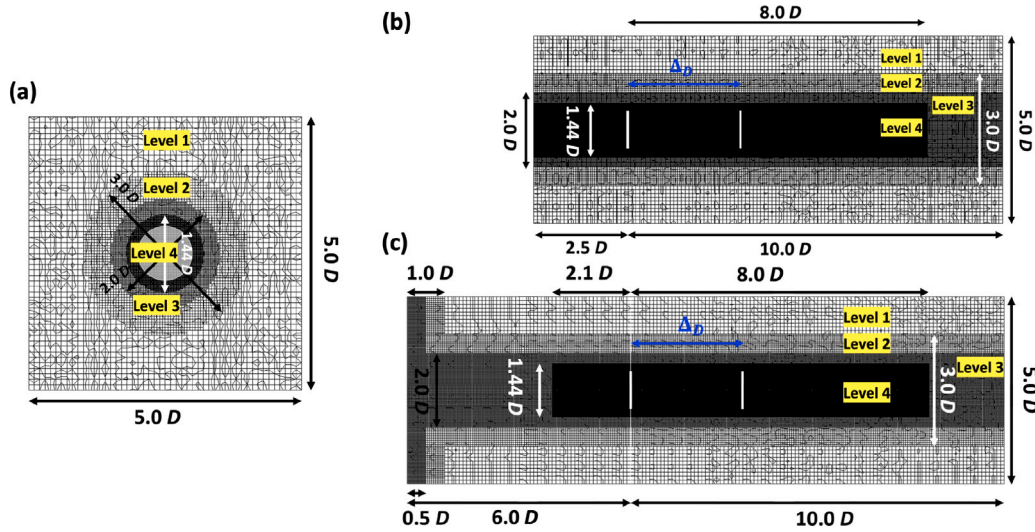
Fig. 2. The mesh layouts for the simulation cases. The upstream rotor is positioned at the origin, the x-position of the downstream rotor is Δ_D, and the two rotors are in tandem. The grid size doubled with a decrease in "Level", and the grid size in Level 4 is $80/D$. (a) is the cross-section of the plane $x = 0$ and is shared by both laminar and turbulent cases. (b) and (c) are the cross sections of plane $y = 0$, where (b) is for the laminar cases (10.4 M cells) while (c) is for the turbulent (10.9 M cells).

surging FOWT rotors with lines of body force fields that rotate and translate (f_{body} in Eq. (8)) [31]. These body force fields are calculated by evaluating the lift and drag forces (L and D) using the blade element approach at the actuator line points (Eqs. (10)–(12)), and then the calculated forces are projected onto the CFD grid through a Gaussian regularization kernel $\eta_\varepsilon(d)$ (Eqs. (13) and (14)). It is noteworthy that the surging velocity V_S (Eq. (4)) has profound effects on the force vectors (f_{2D}) as it alters the magnitudes and directions of f_{2D}. This is because the magnitudes and directions of the relative velocities (V_{rel} in Eq. (11)) are affected by V_S. Also, the positions to project the force fields change naturally according to the surging motions (p_R in Eq. (13) varies if the rotor is surging). See Li et al. [10] for more detailed descriptions.

$$V_{n,\text{app}} = V_n - V_S \tag{10}$$

$$V_{\text{rel}} = \sqrt{V_{n,\text{app}}^2 + (-\Omega r + V_\theta)^2}, \qquad \phi = \arctan\left(\frac{V_{n,\text{app}}}{-\Omega r + V_\theta}\right) = \alpha + \gamma \tag{11}$$

$$f_{2D}(r) = (L, D) = \frac{1}{2}\rho V_{\text{rel}}^2 c\left(C_l(\alpha)\hat{e}_L, C_d(\alpha)\hat{e}_D\right) = f_n\hat{e}_n + f_\theta\hat{e}_\theta \tag{12}$$

$$f_{\text{body}}(x) = \sum_{i=1}^{B}\int_0^R f_{\text{tip}}(r_i)f_{2D}(r_i)\eta_\varepsilon(\|x - (r_i\hat{e}_i + p_R)\|)dr_i \tag{13}$$

$$\eta_\varepsilon(d) = \frac{1}{\varepsilon^3\pi^{3/2}}\exp\left[-\left(\frac{d}{\varepsilon}\right)^2\right] \tag{14}$$

$$f_{\text{tip}}(r) = \frac{2}{\pi}\arccos\left[\exp\left(-\frac{B(R-r)}{2r\sin\phi}\right)\right] \tag{15}$$

Each turbine blade is modeled using 40 actuator line points with equidistant. The grid size Δ of the wake regions (Level 4 in Fig. 2, $\Delta = D/80$) is made to match the distance between the actuator line points Δ_r, and the smoothing factor ε in Eq. (14) is set to 2Δ. These setups follow the recommendations of previous work [13,32]. A tip correction factor f_{tip} based on the Glauert model (Eq. (15)) is implemented to ensure that the loads at the tips/roots of the rotor drop to zero [33]. R and r stand for the rotor radius and the radial distance from the rotor center, respectively. An additional actuator line element is introduced to model the hub with $C_d = 0.3$ and a reference area of πr_{hub}^2, where $r_{\text{hub}} = 1.5$ m is the radius of the hub [34,35]. Note that dynamic stall models and aeroelastic couplings are not implemented.

2.5. Test matrices

Table 1 lists the settings of the simulation cases involving dual rotors. Additionally, for comparative analysis, the table includes four cases featuring a single rotor reported by Li et al. [10], which are presented at the bottom. The column "TI" represents the inflow turbulence intensity (Lam. refers to laminar). The columns "Up" and "Down" indicate the surging configurations of the upstream and downstream rotors (F stands for fixed, and S stands for surging). "Δ_D" indicates the inter-spacing between the two rotors, and "$\Delta_{\phi_{S_0}}$" indicates the phase difference of the surging motions between the two rotors if they are both surging. Note that all the surging rotors for the cases in Table 1 share the same surging settings ($A_S = 4$ m and $\omega_S = 0.63$ rad/s), and the rotational speeds of the upstream and downstream rotors (Ω^{up} and Ω^{down}) are set to Ω_{rated} and $2\Omega_{\text{rated}}/3$, respectively.

For brevity, the table for the test matrix is concatenated with the output quantities related to the time-averaged power coefficients $\overline{C}_P$, which will be discussed in the later sections. Notice that, in this work, the reference velocities for all C_P related quantities are set to the mean freestream velocity 11.4 m/s for convenience. The columns $\overline{C}_P^{\text{up}}$ and $\overline{C}_P^{\text{down}}$ are for the outputted time-averaged power coefficients of the upstream and downstream rotors. The columns "$\overline{G}_{C_P}$" are the gains of $\overline{C}_P$ when compared to the fixed reference cases of the set having the same Δ_D and inflow TI (FF or F- in bold font). Definition of $\overline{G}_{C_P}$ is in Eq. (16). Superscripts up/down/total indicate upstream/downstream/combined, respectively. In all cases examined in this study, the reference velocity of the power coefficients C_P is set to $V_{0,\text{rated}}$ regardless of the apparent inflow velocity seen by the rotors. The overbar notation in this work denotes time-averaging, and the terms time-averaging and mean are used interchangeably.

$$\overline{G}_{C_P} = \frac{\overline{C}_P \text{ of the interested case} - \overline{C}_P \text{ of the \textbf{reference case}}}{\overline{C}_P \text{ of the \textbf{reference case}}} \times 100\% \tag{16}$$

3. Results and discussions

In Sections 3.1 and 3.2, the effects of different fixed–surging configurations (F–S configurations) and phase differences between the surging motions ($\Delta_{\phi_{S_0}}$) are evaluated by analyzing the rotors' performance and wake system. Furthermore, the roles of the inflow conditions and Δ_D are investigated in both subsections. Cases subjected to realistic turbulent inflow conditions (inflow TI = 5.3%) are mainly focused because they more closely mimic the offshore environments. Cases under laminar inflow conditions are also tested and examined to assess the effects of ambient turbulence. However, it should be noted that laminar inflow conditions are generally considered unrealistic out in the field.

Table 1
The settings and the representative results for the simulation cases. The four bottommost cases are simulations with a single rotor from Li et al. [10]. "TI" represents the inflow turbulence intensity (Lam. stands for laminar inflow conditions). "Up" and "Down" indicate whether or not the upstream and downstream rotor is surging (F stands for fixed and S stands for surging). "Δ_D" indicates the inter-spacing between the two rotors. "$\Delta_{\phi_{S_0}}$" denotes the phase difference of the surging motions between the two rotors, see Eq. (3) for the definition. "$\overline{G}_{C_P}$" is the gain of $\overline{C}_P$ when compared to configuration FF or F- (in bold font) of the same set, see Eq. (16) for the definition.

Case	TI [%]	Δ_D/D	Up	Down	$\Delta_{\phi_{S_0}}$ [rad]	$\overline{C}_P^{\mathrm{up}}$	$\overline{C}_P^{\mathrm{down}}$	$\overline{G}_{C_P}^{\mathrm{up}}$ [%]	$\overline{G}_{C_P}^{\mathrm{down}}$ [%]	$\overline{G}_{C_P}^{\mathrm{total}}$ [%]
3L1			**F**	**F**	–	**0.515**	**0.076**	–	–	–
3L2			S	F	–	0.521	0.085	1.1	12.3	2.6
3L3			F	S	–	0.515	0.086	0.0	13.7	1.8
3L4	Lam.	3.0	S	S	0.0π	0.521	0.092	1.1	21.5	3.8
3L5			S	S	0.5π	0.521	0.094	1.2	23.4	4.0
3L6			S	S	1.0π	0.521	0.094	1.2	23.8	4.1
3L7			S	S	1.5π	0.521	0.093	1.2	21.7	3.8
3T1			**F**	**F**	–	**0.516**	**0.138**	–	–	–
3T2			S	F	–	0.524	0.140	1.5	1.6	1.5
3T3			F	S	–	0.516	0.140	0.0	1.4	0.3
3T4	5.3	3.0	S	S	0.0π	0.524	0.141	1.5	2.5	1.7
3T5			S	S	0.5π	0.524	0.140	1.5	1.8	1.5
3T6			S	S	1.0π	0.524	0.142	1.5	3.5	1.9
3T7			S	S	1.5π	0.525	0.142	1.6	3.3	1.9
5L1			**F**	**F**	–	**0.517**	**0.076**	–	–	–
5L2			S	F	–	0.523	0.108	1.1	42.2	6.3
5L3			F	S	–	0.517	0.087	0.0	14.1	1.8
5L4	Lam.	5.0	S	S	0.0π	0.523	0.114	1.1	49.8	7.3
5L5			S	S	0.5π	0.523	0.113	1.1	49.2	7.3
5L6			S	S	1.0π	0.523	0.114	1.1	49.8	7.3
5L7			S	S	1.5π	0.523	0.114	1.1	50.4	7.4
5T1			**F**	**F**	–	**0.518**	**0.181**	–	–	–
5T2			S	F	–	0.525	0.184	1.5	1.6	1.5
5T3			F	S	–	0.518	0.176	0.0	−2.9	−0.7
5T4	5.3	5.0	S	S	0.0π	0.525	0.178	1.5	−1.8	0.7
5T5			S	S	0.5π	0.525	0.177	1.4	−2.1	0.5
5T6			S	S	1.0π	0.525	0.178	1.5	−1.5	0.7
5T7			S	S	1.5π	0.526	0.178	1.5	−1.7	0.7
1* [10]	Lam.	–	**F**	–	–	**0.517**		–	–	–
2* [10]			S			0.523		1.0		
3* [10]	5.3	–	**F**	–	–	**0.518**		–	–	–
4* [10]			S			0.526		1.5		

In addition to the results presented in this manuscript, animations of flow fields sampled on section $y/D = 0$ for most of the cases are available at the corresponding data repository [36].

3.1. Analysis of different fixed–surging rotor configurations

This subsection investigates the cases with different fixed–surging configurations (F–S configurations), covering cases **3L1-3L4**, **3T1-3T4**, **5L1-5L4**, and **5T1-5T4** in Table 1 (16 cases in total). Cases having all four different F–S configurations are tested with both laminar and turbulent (TI= 5.3%) inflow conditions as well as with two inter-spacings Δ_D, which are $3D$ and $5D$ (in this part, $\Delta_{\phi_{S_0}} = 0.0\pi$ is set for SS configuration). The analysis is conducted on the integral properties of wakes (streamwise velocity), rotor (power) performance, two-dimensional contour plots, and three-dimensional isosurfaces. The objective is to provide in-depth knowledge on how surging motions of FOWTs impact the aerodynamics of the wake interaction system.

3.1.1. Integral properties of wake

Fig. 3 presents the profiles of the mean disk-averaged streamwise velocity $\overline{u}_{\mathrm{Disk}}$ in the x-direction for the cases with different F–S configurations. Additionally, four single-rotor cases from Li et al. [10] are included for comparison (cases **1***-**4*** in Table 1), highlighting the impacts of the presence of downstream rotor. Clearly, with the presence of the downstream rotor, $\overline{u}_{\mathrm{Disk}}$ further decreases.

Regarding the effects of different F–S configurations, whether or not the upstream rotor is surging has more pronounced influences than the downstream one for both Δ_D being $3D$ and $5D$, especially for the laminar cases. For the laminar cases, the cases with a surging upstream rotor (configurations SF and SS) have significantly higher values for

$\overline{u}_{\mathrm{Disk}}$ compared to the cases with a fixed upstream rotor (configurations FF and FS) at a given x-position, while whether or not the downstream rotor is surging has much less effects on the profiles of $\overline{u}_{\mathrm{Disk}}$. Regarding the turbulent cases, cases with a surging upstream rotor have slightly larger $\overline{u}_{\mathrm{Disk}}$ profiles compared to cases with a fixed upstream rotor, and the effects of whether or not the downstream rotor is surging are once again less observable.

3.1.2. Rotor performance

Fig. 4 presents the results of the cycle-averaged power coefficients of the upstream and downstream rotors ($\langle C_P^{\mathrm{up}}\rangle$ and $\langle C_P^{\mathrm{down}}\rangle$) for the cases having $\Delta_D = 5D$ with the four different F–S configurations. $\langle C_P^{\mathrm{up}}\rangle$ and $\langle C_P^{\mathrm{down}}\rangle$ for the cases with $\Delta_D = 3D$ are not presented, since they have similar characteristics. The values of $\overline{C}_P^{\mathrm{up}}$ and $\overline{C}_P^{\mathrm{down}}$, which represent the time-averaged rotor power performance, are listed in Table 1. The impacts of the different F–S configurations on $\overline{C}_P^{\mathrm{up}}$ and $\overline{C}_P^{\mathrm{down}}$ are evaluated through $\overline{G}_{C_P}^{\mathrm{up}}$ and $\overline{G}_{C_P}^{\mathrm{down}}$ (gains of $\overline{C}_P^{\mathrm{up}}$ and $\overline{C}_P^{\mathrm{down}}$ due to the surging motions, defined in Eq. (16)), which are presented in the histograms in Fig. 5. The power spectrum of C_P^{down}, denoted as $S_{C_P^{\mathrm{down}}}(f)$, for all 16 cases inspected in this subsection is presented in Fig. 6. This figure illustrates the effects of the upstream rotor on the downstream rotor, particularly when the upstream rotor is surging.

Cycle-averaged C_P of the upstream rotor ($\langle C_P^{\mathrm{up}}\rangle$). Focusing on the cycle-averaged power coefficient of the upstream rotor (Fig. 4(a1) and (b1)), it can be seen that $\langle C_P^{\mathrm{up}}\rangle$ is insensitive to both inflow TI and whether or not the downstream rotor is surging. It is only significantly affected by the surging configuration of the upstream rotor. This is well reflected in the values of $\overline{C}_P^{\mathrm{up}}$ presented in Table 1, in which it shows that, if the other parameters are kept the same, changes in inflow conditions have
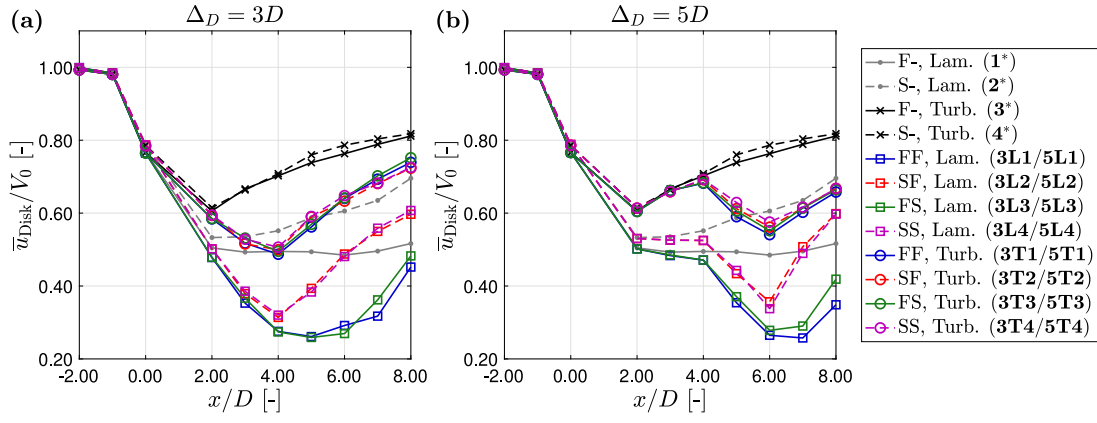
Fig. 3. $\overline{u}_{\mathrm{Disk}}$ profiles for cases having different fixed–surging configurations under laminar/turbulent inflow conditions with different Δ_D. Cases with a surging upstream rotor are plotted in dashed lines, while cases with a fixed upstream rotor are in solid lines. (a) Cases having $\Delta_D = 3D$. (b) Cases having $\Delta_D = 5D$.
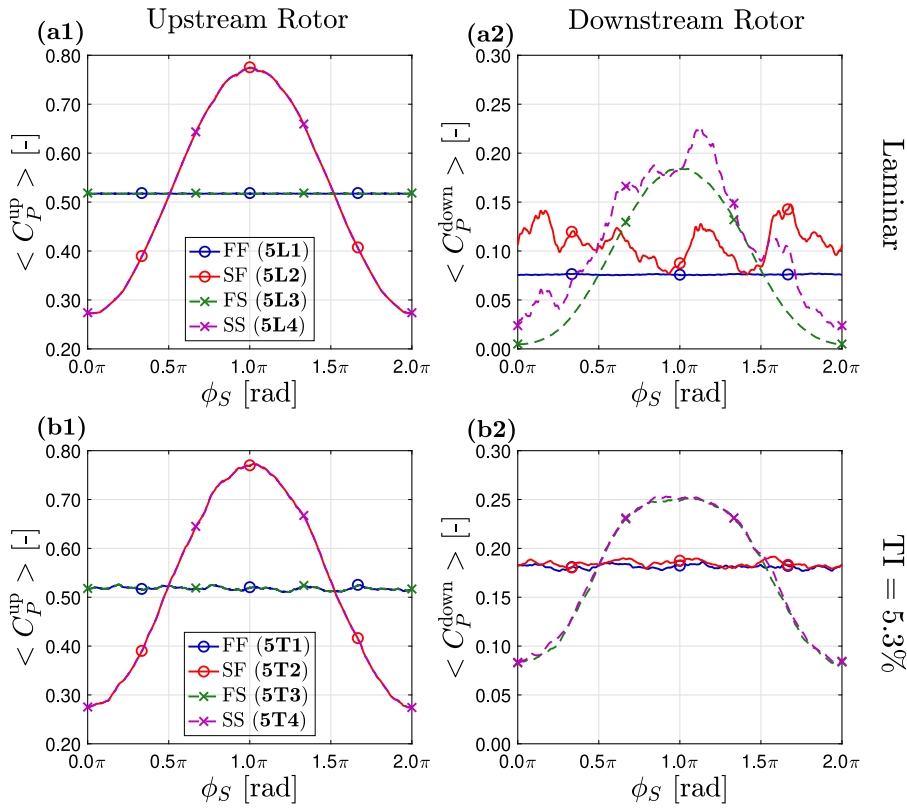

Fig. 4. Cycle-averaged power performance of the two rotors ($\langle C_P^{\mathrm{up}} \rangle$ and $\langle C_P^{\mathrm{down}} \rangle$) for the cases with the four different F–S configurations. The spacings (Δ_D) of these cases are $5D$. (a): Cases under laminar inflow conditions. (b): Cases under turbulent inflow conditions (TI = 5.3%).

a rather limited impact on $\overline{C}_P^{\mathrm{up}}$. This finding is in accordance with what Li et al. reported [10]. Additionally, when the surging configuration and the inflow conditions are identical, the values of $\overline{C}_P^{\mathrm{up}}$ in Table 1 also show that they are insensitive to the placement of the downstream rotor and its surging configuration. Compared to the single rotor cases (cases **1***-**4***), the placement of the downstream rotor only decreases $\overline{C}_P^{\mathrm{up}}$ by ~0.3% and ~0.02% when Δ_D is $3D$ and $5D$, respectively. Similar to fixed wind turbine rotors [37], these results show that surging wind turbine rotors also have negligible effects on upstream flows as the distances are sufficiently large ($\geq 3D$).

Cycle-averaged C_P of the downstream rotor ($\langle C_P^{\mathrm{down}} \rangle$). Unlike $\langle C_P^{\mathrm{up}} \rangle$, the curves of $\langle C_P^{\mathrm{down}} \rangle$ for the laminar cases in Fig. 4(a2) are not only

affected by the surging configuration of the downstream rotor but are also significantly influenced by the surging configuration of the upstream rotor. Considering the laminar cases that have the same surging configuration for the downstream rotor, those with a surging upstream rotor (configurations SF and SS) have significantly higher $\langle C_P^{\mathrm{down}} \rangle$ compared to those with a fixed upstream rotor (configurations FF and FS). This is clearly reflected on the values of $\overline{C}_P^{\mathrm{down}}$ and $\overline{G}_{C_P}^{\mathrm{down}}$ presented in Table 1 and Fig. 5.

In the turbulent cases, the response of $\langle C_P^{\mathrm{down}} \rangle$ in Fig. 4(b2) shows reduced sensitivity to the surging configuration of the upstream rotor compared to the laminar cases. Instead, these curves primarily depend on the surging configuration of the downstream rotor. This indicates
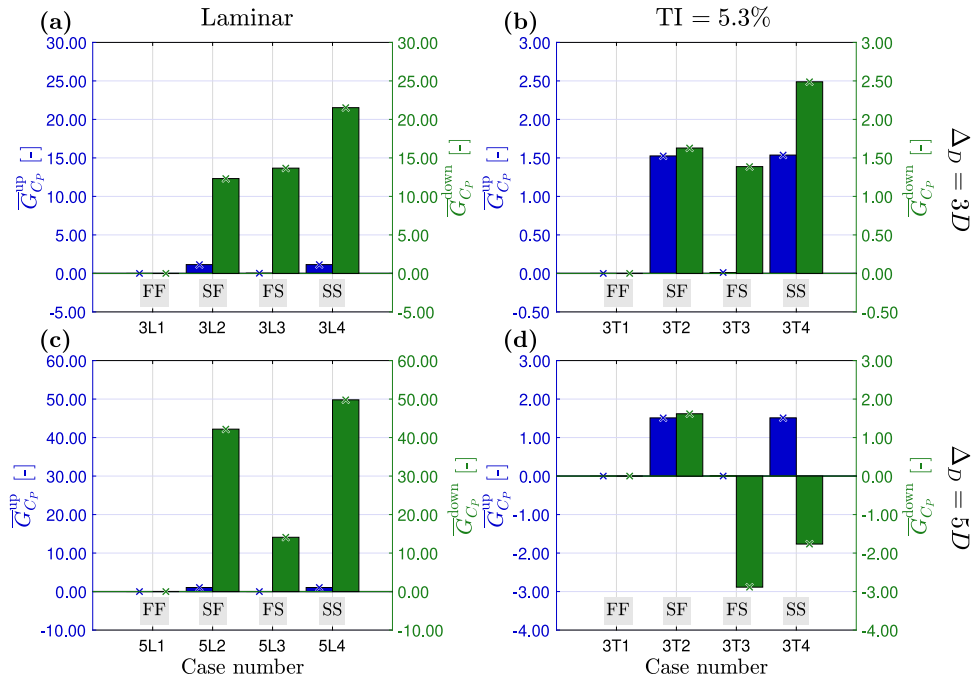
Fig. 5. Gains on the time-averaged power coefficients of the upstream and downstream rotor compared to configuration FF ($\overline{G}_{C_P}^{\text{up}}$ and $\overline{G}_{C_P}^{\text{down}}$, which are in blue and in green, respectively) for the cases with the four different F–S configurations. Definition of $\overline{G}_{C_P}$ is in Eq. (16). Ticks of the horizontal axis denote the case numbers introduced in Table 1. Cases in each panel share the same Δ_D and inflow conditions. The cases in the top and bottom rows have $\Delta_D = 3D$ and $5D$, respectively. The cases plotted in the left and right columns are subjected to laminar and turbulent (TI =5.3%) inflow conditions, respectively.
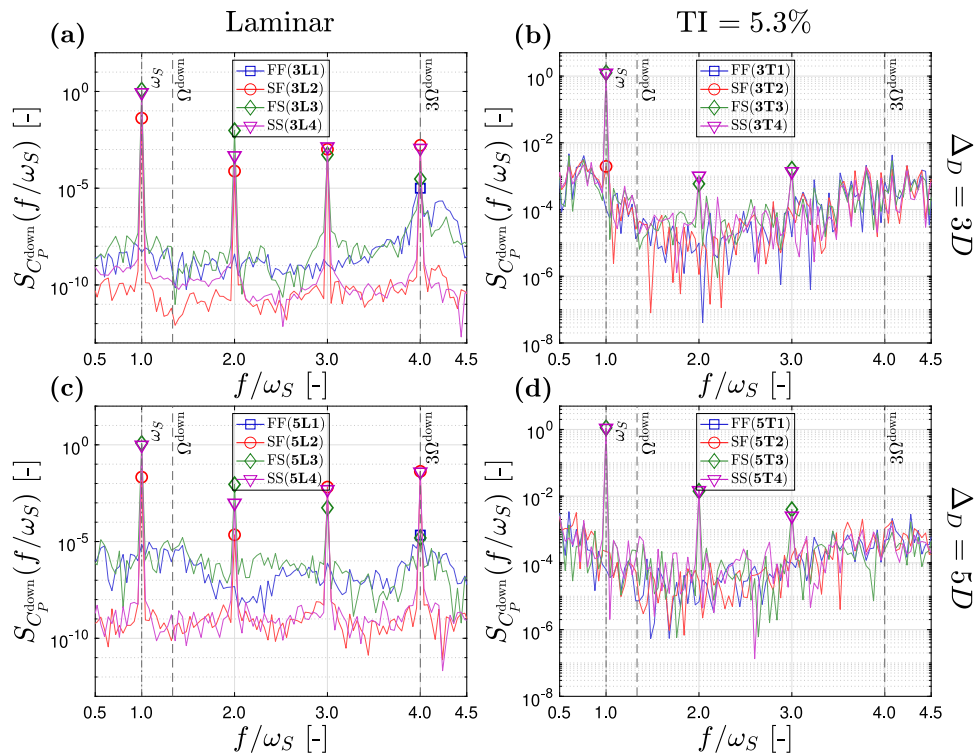

Fig. 6. The power spectrum of the downstream rotor's power coefficient ($S_{C_P^{\text{down}}}$) for the cases with four different F–S configurations. The peaks are labeled with markers if they are clearly identified. Cases plotted in the top and bottom rows have $\Delta_D = 3D$ and $5D$, respectively. Cases plotted in the left and right columns have laminar and turbulent (TI =5.3%) inflow conditions, respectively. ω_S corresponds to the surging frequency and Ω^{down} is the rotational frequency of the downstream rotor.
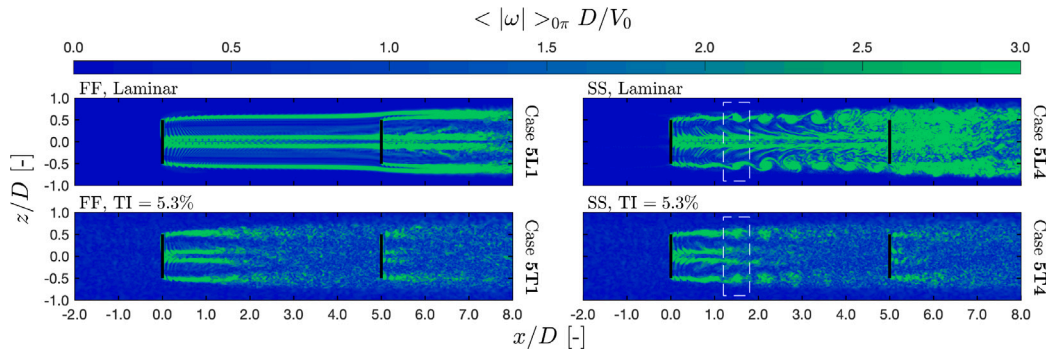
Fig. 7. Contours of phase-averaged vorticity magnitude $\langle|\omega|\rangle_{0\pi}$ of the selected cases with $\Delta_D = 5D$. Upper row: Cases with configuration FF and SS subjected to laminar inflow conditions. Lower row: Cases with configuration FF and SS subjected to turbulent inflow conditions (TI = 5.3%). The case numbers are labeled on the right of each panel. Example sets of SIPeCS identified in the SS cases are enclosed in boxes of dashed lines.

that, compared to the cases subjected to laminar inflow conditions, the surging configuration of the upstream rotor is much less relevant to the downstream rotor when the inflow conditions are turbulent. However, even though not obvious with the curves of $\langle C_P^{\text{down}}\rangle$, the surging configuration of the upstream rotor still has noticeable impacts on the values of $\overline{C}_P^{\text{down}}$, which will be shown and discussed in the following paragraphs.

Gains in time-averaged C_P due to the surging motions ($\overline{G}_{C_P}^{\text{up}}$ and $\overline{G}_{C_P}^{\text{down}}$). Impacts of the different F–S configurations on both $\overline{C}_P^{\text{up}}$ and $\overline{C}_P^{\text{down}}$ are evaluated through $\overline{G}_{C_P}^{\text{up}}$ and $\overline{G}_{C_P}^{\text{down}}$ plotted in Fig. 5 (their values can also be found in Table 1). These panels are organized based on inflow conditions and Δ_D, enabling a detailed examination of the interplay between these factors and different F–S configurations. Note that $\overline{G}_{C_P}^{\text{up}}$ and $\overline{G}_{C_P}^{\text{down}}$ are evaluated by comparing the cases with configuration FF that have the same inflow conditions and Δ_D.

Similarly to what is observed with the curves of $\langle C_P^{\text{up}}\rangle$, the four panels of Fig. 5 show that $\overline{G}_{C_P}^{\text{up}}$ are insensitive to the downstream rotor's surging configuration. Furthermore, $\overline{G}_{C_P}^{\text{up}}$ is consistently around positive $1.1 \sim 1.5\%$ if the upstream rotor is surging for both laminar and turbulent inflow conditions, reaffirming the finding and analysis of the previous studies [7,10].

Unlike $\overline{G}_{C_P}^{\text{up}}$, the values of $\overline{G}_{C_P}^{\text{down}}$ are not only affected by the surging configuration of the downstream rotor but they are also affected by whether or not the upstream rotors are surging, particularly for the cases subjected to laminar inflow conditions. For the laminar cases with a surging upstream rotor (configurations SF and SS), their $\overline{G}_{C_P}^{\text{down}}$ are profoundly higher compared to the cases with a fixed upstream rotor (configurations FF and FS). Particularly, the values of their $\overline{G}_{C_P}^{\text{down}}$ are around 10% and 40% higher for the cases with $\Delta_D = 3D$ and $5D$, respectively. Regarding the cases subjected to turbulent inflow conditions, although not as significant as the laminar cases, $\overline{G}_{C_P}^{\text{down}}$ is again higher for configurations SF and SS compared to configurations FS and FF (by around $1.0 \sim 1.5\%$). These show that the downstream rotor's power performance is better if the upstream rotor is surging than if it is fixed. Furthermore, it is worth pointing out that the values of $\overline{C}_P^{\text{up}}$ are already higher for a surging upstream rotor compared to a fixed upstream rotor. The findings here indicate that, although only slightly when the inflow conditions are turbulent with realistic TI, the surging motion of the upstream rotor enhances its wake recovery and is beneficial for the overall power output of the considered dual-rotor system.

Regarding the effects of the downstream rotor's surging configurations on $\overline{G}_{C_P}^{\text{down}}$, they are significantly different for the two considered Δ_D. Focusing on the cases with inflow TI = 5.3%, $\overline{C}_P^{\text{down}}$ for the cases having $\Delta_D = 3D$ are higher if the downstream rotors are surging

(i.e., $\overline{C}_P^{\text{down}}$ for configurations FS or SS are higher than that of configurations FF or SF), while the opposite happens for the cases having $\Delta_D = 5D$, where their $\overline{G}_{C_P}^{\text{down}}$ are negative. These are related to the fact that the operational conditions (Ω^{down}) are prescribed (based on the rough estimations of inflow velocity, which are 7.6 m/s for both $\Delta_D = 3D$ and $5D$) and no controlling strategies are implemented. However, considering $\overline{C}_P^{\text{down}}$ for cases with $\Delta_D = 3D$ under turbulent inflow are enhanced by the surging motion of the downstream rotor, the power outputs for the downstream rotor could be benefited by its surging motion if it is properly controlled (see Li et al. [38] for detailed discussions).

Power spectrum of C_P^{down} ($S_{C_P^{\text{down}}}$). The power spectrum of C_P^{down} ($S_{C_P^{\text{down}}}$) for the 16 cases are presented in Fig. 6 with four separated panels based on their inflow conditions (laminar/turbulent) and Δ_D ($3D/5D$). Three characteristic frequencies are labeled on the plots with vertical dashed lines, which are the surging frequency (ω_S), downstream rotor's rotational frequency (Ω^{down}), and three times of Ω^{down} ($3\Omega^{\text{down}}$). The factor 3 of the last relates to the 120° rotor symmetry (corresponding to the so-called "3P" [39]). Given the rotors' perfect 120° symmetry and near axisymmetric inflow, the "3P" ($3\Omega^{\text{down}}$) signal is expected, and indeed observed, to be more prominent than the "1P" (Ω^{down}) signal (the signal of the latter is not clearly detected in all cases presented).

Focusing on the frequency of $3\Omega^{\text{down}}$ (relates to the rotation of the rotor) for the cases with configuration FF, the cases with laminar inflow have clear and sharp peaks for configuration FF (cases **3L1** and **5L1**), while the peaks for the cases also having configuration FF but with turbulent inflow conditions (cases **3T1** and **5T1**) are absent. In the laminar cases, the 3P signal arises due to wake structures from the upstream rotor (slightly) disrupting the system's axisymmetry. For turbulent cases with configuration FF, ambient turbulence dissipates these upstream wake structures, restoring axisymmetry, and as a result, the 3P signal does not clearly appear.

Regarding the frequency of ω_S (relates to the surging motion), very clear peaks at $f = \omega_S$ in $S_{C_P^{\text{down}}}$ can be found for the cases with a surging downstream rotor regardless of the inflow conditions and values of Δ_D. Furthermore, for the cases with laminar inflow (see Fig. 6(a) and (c)), even if the downstream rotor is fixed, the peaks at $f = \omega_S$ still obviously occur if the upstream rotor is surging (configuration SF, with lower peak values compared to configurations FS and SS), while the peaks at $f = \omega_S$ are absent for the cases with configuration FF. This suggests that, as the inflow conditions are laminar, the impacts of the SIPeCS (Surge-Induced Periodic Coherent Structures, see Fig. 9) shed by the surging upstream rotor are significant. However, if the inflow conditions are switched to turbulent (TI = 5.3%, Fig. 6(b) and (d)), the peak value at $f = \omega_S$ for the case with configuration SF having $\Delta_D = 3D$ becomes rather small, and the peak for configuration SF having $\Delta_D = 5D$ is virtually not recognizable. This observation shows that the

impacts of SIPeCS shed by the surging upstream rotor are gradually diminished by ambient turbulence as SIPeCS travels downstream.

For the harmonics of ω_S ($2\omega_S$, $3\omega_S$, $4\omega_S$, ..., and note that $4\omega_S = 3\Omega^{\mathrm{down}}$), peaks are clearly visible at those frequencies for the cases with configurations FS, SS, and SF when under laminar inflow conditions. On the other hand, when under turbulent inflow conditions, these peaks become much less pronounced (FS and SS) or undetectable (SF).

3.1.3. Contours of phase averaged vorticity magnitude $\langle|\omega|\rangle_{0\pi}$

The aim of this part is to identify the impacts of surging motions by inspecting the flow structures using contours of phase-averaged vorticity magnitude $\langle|\omega|\rangle_{0\pi}$. $\langle|\omega|\rangle_{0\pi}$ fields are obtained by averaging the instantaneous vorticity ($|\omega|$) fields sampled with the surging frequency ω_S, as it is defined and explained in Section 2.2. As demonstrated by Li et al. [10], contours of $\langle|\omega|\rangle_{0\pi}$ are capable of effectively illustrating the flow structures induced by harmonic surging FOWT, and they called these distinct flow structures *Surge-Induced Periodic Coherent Structures* (SIPeCS). As expected, SIPeCS are again identified in the current work, where example sets of SIPeCS are enclosed in dashed-line boxes in Fig. 7.

For brevity, only the four most representative cases are plotted with their phase-averaged vorticity fields in Fig. 7, and comparative analysis will be carried out based on it in the following paragraphs. The four cases are the laminar and turbulent cases with configuration FF and SS (cases **5L1**, **5L4**, **5T1**, and **5T4**). All four cases have $\Delta_D = 5D$. Configurations SF and FS are not plotted, as they are less relevant for the real-world wind farm. While for the cases having $\Delta_D = 3D$, their general features of $\langle|\omega|\rangle_{0\pi}$ are similar to those having $\Delta_D = 5D$. More comprehensive presentations of flow fields are available at the corresponding data repository [36], where animations of instantaneous out-of-plane vorticity fields ω_y and streamwise velocity fields u are provided for all the 16 cases presented in this subsection.

Before starting the analysis, it is worth noting that the phase-averaged flow fields for the cases under laminar conditions, while being the average of several samples, are highly reminiscent of the instantaneous flow fields even when both rotors are surging. This is due to the fact that the flow fields are highly repeatable with respect to ω_S when ambient turbulence is absent. See Appendix A for further analysis and discussions on this based on the phase-averaged turbulent kinetic energy fields.

First, focus on the two cases under laminar inflow conditions in Fig. 7 (upper row), where the contours of the (phase-averaged) vortical structures are clearer and sharper than those of the turbulent cases (lower row). Looking at the cases with configuration FF (case **5L1**), it can be seen that the vortex tubes (degenerated from helical structures) released by the upstream and downstream rotors interact around 1-2D downstream away from the downstream rotor, smearing out the sharp contours and indicating the initiative of the wake breakdown. This is consistent with the finding of Troldborg [32]. It is worth noting that for configuration FS (case **5L3**), even though SIPeCS of the downstream rotor are spotted (in smaller sizes, see the corresponding data repository [36]), there is no earlier onset of the wake breakdown observed for the dual rotor system compared to configuration FF. For configuration SS (case **5L4**), the large vortical structures induced by the surging motions, namely SIPeCS, can be clearly identified, displaying the effects of surging on the wake aerodynamics. As comparing the $\langle|\omega|\rangle_{0\pi}$ fields of configuration SS (case **5L4**) to configuration SF (case **5L2**, see the corresponding data repository [36]), it is found that the two cases share very similar contours. This shows that the SIPeCS shed by the upstream rotor strongly dominates the induction fields, whereas the SIPeCS induced by the downstream rotor has less impact. Additionally, it can be seen that the SIPeCS shed by the upstream rotor remain clear and sharp as they reach the downstream rotor, and this has already been reflected on the spectra of C_P^{down} presented in Fig. 6, where peaks at $f = \omega_S$ appear sharply for the laminar cases with configuration SF even if the downstream rotors are fixed.

Next, for the cases with turbulent inflow conditions (TI= 5.3%, cases **5T1-5T4**), their $\langle|\omega|\rangle_{0\pi}$ fields appear to depend only on whether the upstream rotor is surging. The downstream rotors all have strips of high vorticity in similar form and at similar positions (the $\langle|\omega|\rangle_{0\pi}$ fields of configurations FF and SS are shown in the lower row of Fig. 7, while SF and FS are not shown for brevity). The major difference among the four cases is that SIPeCS can be identified between the two rotors for configurations SF and SS but not in configurations FF and FS. Unlike the laminar cases, whether or not the downstream rotor is surging does not have perceivable effects on the $\langle|\omega|\rangle_{0\pi}$ fields, indicating that the strengths of the SIPeCS shed by the downstream rotor are not strong enough to prevent them from being smeared by the turbulence. This can be attributed to the fact that the loading of the downstream rotor is smaller compared to the upstream rotor, and the turbulence experienced by it is stronger since the downstream rotor operates in the wake of the upstream rotor [32,40]. Moreover, for the turbulent cases with $\Delta_D = 3D$, the structures of SIPeCS shed by the upstream rotor remain clear as they hit the downstream rotor based on the phase-averaged vorticity fields. However, SIPeCS are more diffused before hitting the downstream rotor for the cases with $\Delta_D = 5D$. This has also been reflected with $S_{C_P^{\mathrm{down}}}$ of the turbulent cases with configuration SF presented in Fig. 6 (the peak at $f = \omega_S$ exists for $\Delta_D = 3D$ but not for $\Delta_D = 5D$). This statement is further supported by the analysis in Section 3.2.

3.1.4. Contours of turbulent kinetic energy TKE

This part examines the (resolved) turbulent kinetic energy (TKE) fields across different fixed–surging configurations to determine whether these configurations influence TKE (definition of TKE is provided in Appendix A). In general, TKE serves as an indicator that reflects the flow velocity fluctuation extent. Additionally, TKE has its practical importance in wind farm aerodynamics as it is one of the key parameters that affect wake recovery rates and the fatigue lifetimes of the downstream turbines [14].

Similarly, for the sake of brevity, only the TKE fields of the same four cases as in Fig. 7 are shown in this part, which is presented in Fig. 8. Note that, unlike phase-averaged properties, (e.g., $\langle|\omega|\rangle_{0\pi}$), which are calculated at the specific time steps, TKE includes all available time steps. For completeness, fields of phase-averaged TKE, denoted as $<TKE>_{0\pi}$, are provided in Appendix A, which focus on the variations of the velocity fields where the effects periodic fluctuations are excluded.

Focusing on the two cases subjected to laminar inflow (top row of Fig. 8), it can be observed that the case with configuration FF (case **5L1**) exhibits relatively low TKE fields up to 1D downstream away from the downstream rotor, indicating limited temporal flow fluctuations. Beyond 1D downstream, TKE values begin to increase (same for the $<TKE>_{0\pi}$ fields of case **5L1** in Fig. A.1), marking the onset of wake breakdown. In contrast, configuration SS (case **5L4**) shows two strips of elevated TKE right after the upstream rotor. These high TKE regions are attributed to the advection of SIPeCS, as the periodic passage of these coherent structures induces temporal velocity fluctuations. However, despite these regions having significant TKE, the wake breakdown process is considered absent until 1D downstream away from the downstream rotor for configuration SS with laminar inflow. Li et al. [10] have noted that the wake flows of a surging wind turbine rotor under laminar conditions fluctuate in a highly periodic manner with minimal randomness (supported by the phase-averaged TKE, denoted as $<TKE>_{0\pi}$, presented in Appendix A). They further emphasized that the enhanced wake recovery rates in a surging FOWT rotor result from improved advection rather than increased turbulent entrainment. Therefore, the TKE contours presented for these two laminar inflow cases should be interpreted with particular caution, since higher TKE values are typically linked to stronger random/stochastic fluctuations that result in faster wake recovery.
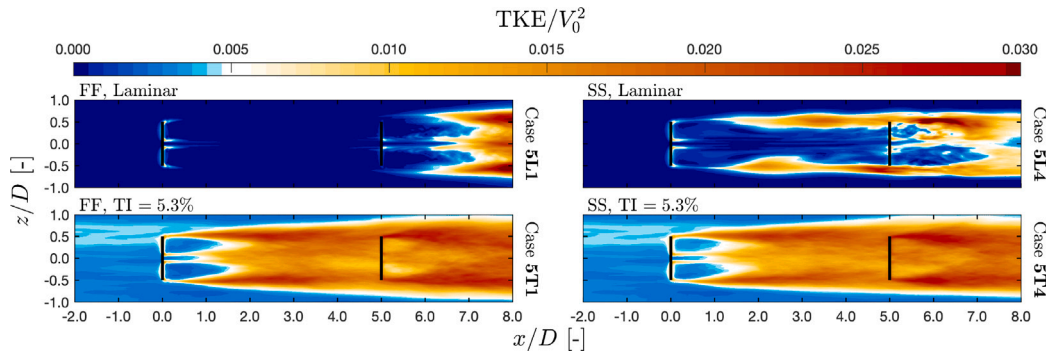
Fig. 8. Contours of turbulent kinetic energy (TKE) of the selected cases with $\Delta_D = 5D$. Upper row: Cases with configuration FF and SS subjected to laminar inflow conditions. Lower row: Cases with configuration FF and SS subjected to turbulent inflow conditions (TI = 5.3%). The case numbers are labeled on the right of each panel.
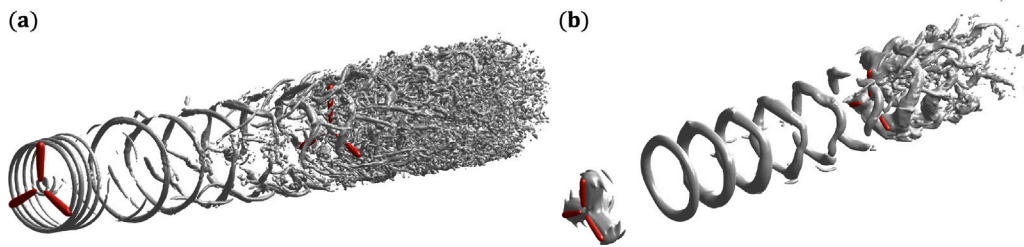

Fig. 9. Iso-surfaces depicting the three-dimensional instantaneous flow structures of surging FOWT rotors subjected to laminar inflow conditions (case **5L4**), in which SIPeCS are clearly depicted. ϕ_S^{up} and ϕ_S^{down} in this time instance are 0.0π. The red surfaces are the body forces projected by the actuator lines ($f_{\text{body},x}/\rho = -5$ N kg^{-1}), which are used to illustrate the rotors. Silver surfaces in (a) and (b) are the iso-surfaces of Q-criterion ($Q = 0.15$ s^{-2}) and kinematic pressure ($\Delta p/\rho = -8$ Pa m^3 kg^{-1}), respectively.

Shifting the attention to the cases subjected to turbulent inflow (bottom row of Fig. 8), it can be seen that the TKE values in the inflow regions align well with the reported inflow turbulence intensity (TI =5.3% corresponds to TKE/V_0^2 = 0.004). In the TKE contour for configuration FF (case **5T1**), strips of elevated TKE values first appear right behind the tip and root regions and then expand, which is consistent with the previous experimental and numerical studies [41]. Comparing the TKE fields of cases with configurations FF and SS, in contrast to the laminar inflow cases, we find that both configurations exhibit almost identical patterns in the dual-rotor system. TKE field values for both of the cases are enhanced as the flow passes the upstream rotor and are further intensified upon passing the downstream rotor. This observation extends the findings of the earlier works [42,43], which showed that the TKE patterns in the wake of a standalone FOWT rotor are similar whether the rotor is fixed or in motion.

3.1.5. Three-dimensional flow structures

This part explores the three-dimensional flow structures of dual surging FOWT rotors, focusing on case **5L4**. This case has SS configuration, Δ_D being $5D$, and is subjected to laminar inflow conditions. Cases subjected to turbulent inflow are not presented due to the noise of turbulence. The main focus is on the three-dimensional visualization of SIPeCS shed by the upstream rotor and their interaction with the downstream rotor. The iso-surfaces of the Q-criterion (Eqs. (17)–(18)) and pressure (Δp, deviations from the ambient pressure) are illustrated in Fig. 9. The iso-surfaces of the Q-criterion, depicted in Fig. 9(a), clearly reveal the helical structures representing the tip and root vortices of the upstream rotor. This visualization demonstrates that the simulations can resolve fine wake structures with high fidelity. As these helical structures travel downstream from the upstream rotor, they quickly decay. Further downstream, the ring structures form. These ring structures also appear in the iso-surfaces of pressure (Fig. 9(b)), where they are depicted more clearly. These ring structures represent SIPeCS that have already been presented with the contour plots in Section 3.1.3, where they are presented in a two-dimensional fashion. Note that vorticity cores with high magnitudes come with low-pressure

cores. As expected, these ring structures are absent in the cases with fixed rotors (e.g., configurations FF, not shown). Furthermore, the SIPeCS-related ring structures depicted in Fig. 9, although deformed, persist after passing the surging downstream rotor. This indicates that the surging motion of the downstream rotor has limited effects on these structures, aligning with previous observations discussed earlier in this work.

$$Q = \frac{1}{2}\left(\Omega_{pq}\Omega_{pq} - S_{pq}S_{pq}\right) \tag{17}$$

$$\Omega_{pq} = \frac{1}{2}\left(\frac{\partial u_p}{\partial x_q} - \frac{\partial u_q}{\partial x_p}\right), \qquad S_{pq} = \frac{1}{2}\left(\frac{\partial u_p}{\partial x_q} + \frac{\partial u_q}{\partial x_p}\right) \tag{18}$$

3.2. Analysis of the phase differences between the two surging motions

This subsection explores the effects of the phase differences of surging motions between the two surging rotors ($\Delta_{\phi_{S_0}}$). The phase difference, $\Delta_{\phi_{S_0}}$, has a practical importance when it comes to the wake interactions inside floating offshore wind farms. It is worth reminding that in our study, $\Delta_{\phi_{S_0}}$ defined in Eq. (3) depends solely on the surging motions of the two rotors and is independent of other parameters, such as Δ_D. Also, $\Delta_{\phi_{S_0}}$ in this work is adjusted by varying the initial phase shift of the upstream rotor's surging motion ($\phi_{S_0}^{\text{up}}$, see Eq. (1)), while initial phase shift for the downstream rotor ($\phi_{S_0}^{\text{down}}$) is always kept as 0.0π. Cases **3L4-3L7**, **3T4-3T7**, **5L4-5L7**, and **5T4-5T7** in Table 1 are interested in this part. However, since the cases with turbulent inflow conditions (TI = 5.3%) are more relevant to real-world applications, investigations are emphasized on turbulent cases (TI = 5.3%). The cases subjected to laminar inflow conditions are conducted as a benchmark and summarized in Table 1 and Appendix B. The effects of $\Delta_{\phi_{S_0}}$ are evaluated with the power outputs of the two rotors ($\overline{C}_P^{\text{up}}$ and $\overline{C}_P^{\text{down}}$), especially with the downstream one. Analysis of the flow structures is also performed to support the findings, which is performed using phase-averaged circulation fields ($\langle \Gamma \rangle_{0\pi}$), a technique introduced by Li et al. [10] used to identify and quantify the positions and strengths of SIPeCS.
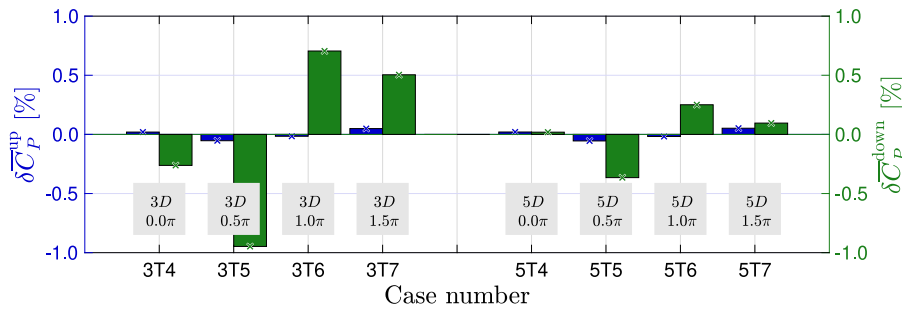
Fig. 10. $\delta \overline{C}_P^{\text{up}}$ and $\delta \overline{C}_P^{\text{down}}$ (relative differences of $\overline{C}_P^{\text{up}}$ and $\overline{C}_P^{\text{down}}$, defined in Eq. (19)) for the SS cases with different $\Delta_{\phi_{S_0}}$ under turbulent inflow conditions (TI= 5.3%). The top entry stands for inter-spacing Δ_D and the bottom stands for the phase difference of the surging motions between the two rotors ($\Delta_{\phi_{S_0}}$, in radians). The averaged values for calculating $\delta \overline{C}_P$ of the four left/right cases are based on themselves (Eq. (19)).

3.2.1. Rotor performances

The relative differences of the time-averaged power outputs of the upstream/downstream rotors ($\delta \overline{C}_P^{\text{up/down}}$) are analyzed in this subsection. The definition of $\delta \overline{C}_P$ is in Eq. (19), where the denominator ($\sum_{i=1}^N \overline{C}_{P,i}^{\text{up/down}} / N$) is the averaged value calculated with the cases having the same Δ_D and subjected to the same inflow conditions. For example, to obtain $\delta \overline{C}_P^{\text{up/down}}$ for the turbulent cases with configuration SS and $\Delta_D = 3D$, $\sum_{i=1}^N \overline{C}_{P,i}^{\text{up/down}} / N$ is calculated by averaging $\overline{C}_P^{\text{up/down}}$ of cases **3T4-3T7** (here $N = 4$ since four $\Delta_{\phi_{S_0}}$ are considered in this work).

Fig. 10 displays the bar graph of $\delta \overline{C}_P$ against different $\Delta_{\phi_{S_0}}$ for the turbulent cases (inflow TI= 5.3%) having $\Delta_D = 3D$ and $5D$. It is clear that $\overline{C}_P^{\text{up}}$ is less sensitive to $\Delta_{\phi_{S_0}}$ compared to $\overline{C}_P^{\text{down}}$. However, it should be noticed that the values of $\delta \overline{C}_P^{\text{down}}$ for the cases presented in Fig. 10 are all within $\pm 1\%$. By comparing the cases with $\Delta_D = 3D$ with the cases having $5D$, it is clear that the magnitudes of $\delta \overline{C}_P^{\text{down}}$ for the cases with $\Delta_D = 5D$ are significantly smaller than those of $\Delta_D = 3D$ (which are down from less than 1.0% to less than 0.4%), pointing out that the influences of $\Delta_{\phi_{S_0}}$ on the downstream rotor decrease with larger Δ_D.

$$\delta \overline{C}_P^{\text{up/down}} = \frac{\overline{C}_P^{\text{up/down}} - \sum_{i=1}^N \overline{C}_{P,i}^{\text{up/down}} / N}{\sum_{i=1}^N \overline{C}_{P,i}^{\text{up/down}} / N} \times 100\% \qquad (19)$$

3.2.2. Positions and strengths of SIPeCS

In this part, effects of $\Delta_{\phi_{S_0}}$ are investigated based on the positions and strengths of SIPeCS through analyzing phase-averaged circulation $\langle \Gamma \rangle_{0\pi}$ fields on the upper half ($z/D \geq 0$) of the $y/D = 0$ plane. Li et al. [10] have shown that based on where the local maxima of $\langle \Gamma \rangle_{0\pi}$ (denoted as $\langle \Gamma \rangle_{0\pi,\text{max}}$) are found, the positions of SIPeCS can be characterized. The strengths of SIPeCS can be characterized by $\langle \Gamma_w \rangle_{0\pi,\text{max}}$, which is $\langle \Gamma \rangle_{0\pi,\text{max}}$ after removing the effects of the shear layer. Definitions of $\langle \Gamma \rangle_{0\pi}$, $\langle \Gamma_u \rangle_{0\pi}$, and $\langle \Gamma_w \rangle_{0\pi}$ used in this work are in Eqs. (20)–(22), and $\langle \Gamma_u \rangle_{0\pi,\text{max}}$ and $\langle \Gamma_w \rangle_{0\pi,\text{max}}$ are both calculated at the positions where $\langle \Gamma \rangle_{0\pi,\text{max}}$ are found. Notice that, on $y/D = 0$ plane, $\langle \Gamma_u \rangle_{0\pi} + \langle \Gamma_w \rangle_{0\pi} = \langle \Gamma \rangle_{0\pi}$. Same as Li et al. [10], $\langle \Gamma \rangle_{0\pi}$ are obtained through integrating circular paths. The radii of the circular paths are $r_\Gamma = 0.15R$, which is roughly just larger than the vortical structures (SIPeCS) observed in Fig. 7. For more detailed descriptions of the methods used to obtain $\langle \Gamma \rangle_{0\pi}$ related quantities and their relevance to SIPeCS, refer to Li et al. [10].

$$\langle \Gamma \rangle_{0\pi} \Big|_{(x=x_0,y=0,z=z_0)} \stackrel{\Delta}{=} \oint_{r=r_\Gamma} (\langle u \rangle_{0\pi}, \langle v \rangle_{0\pi}, \langle w \rangle_{0\pi}) \cdot \mathrm{d}\boldsymbol{l}$$

$$= \int_A \nabla \times (\langle u \rangle_{0\pi}, \langle v \rangle_{0\pi}, \langle w \rangle_{0\pi}) \cdot \mathrm{d}\boldsymbol{A} = \int_A \langle \omega_y \rangle_{0\pi} \, \mathrm{d}A \qquad (20)$$

$$\langle \Gamma_u \rangle_{0\pi} \Big|_{(x=x_0,y=0,z=z_0)} \stackrel{\Delta}{=} \oint_{r=r_\Gamma} (\langle u \rangle_{0\pi}, 0, 0) \cdot \mathrm{d}\boldsymbol{l} \qquad (21)$$

$$\langle \Gamma_w \rangle_{0\pi} \Big|_{(x=x_0,y=0,z=z_0)} \stackrel{\Delta}{=} \oint_{r=r_\Gamma} (0, 0, \langle w \rangle_{0\pi}) \cdot \mathrm{d}\boldsymbol{l} \qquad (22)$$

The values of $\langle \Gamma \rangle_{0\pi,\text{max}}$, $\langle \Gamma_u \rangle_{0\pi,\text{max}}$, and $\langle \Gamma_w \rangle_{0\pi,\text{max}}$ are plotted against the x-positions where $\langle \Gamma \rangle_{0\pi,\text{max}}$ are found in Figs. 11 and 12. The cases with $\Delta_{\phi_{S_0}}$ being 0.0π, 0.5π, 1.0π, and 1.5π are plotted along with the reference cases (configuration FF). The cases having $\Delta_D = 3D$ are displayed in Fig. 11 while those having $\Delta_D = 5D$ are displayed in Fig. 12. All the cases are subjected to turbulent inflow conditions of TI = 5.3%. Note that the subscript "0π" for phase-averaged quantities, such as $\langle \Gamma \rangle_{0\pi}$, corresponds specifically to ϕ_S^{down} (surging phase angle of the downstream rotor, $\phi_{S_0}^{\text{down}}$ in Eq. (2), is always kept 0.0π in this work) in this subsection.

The x-positions where the maximum values of $\langle \Gamma \rangle_{0\pi}$ are found are presented in Figs. 11(a) and 12(a), which correspond to the x-positions of the SIPeCS, exhibit a strong correlation with the values of $\Delta_{\phi_{S_0}}$. Specifically, when scanning in the positive x-direction, the x-positions of $\langle \Gamma \rangle_{0\pi,\text{max}}$ (i.e., the SIPeCS's x-positions) for cases with smaller $\Delta_{\phi_{S_0}}$ are detected earlier compared to cases with larger $\Delta_{\phi_{S_0}}$. This pattern holds consistently up to the downstream rotor, both for the cases with $\Delta_D = 3D$ and $5D$.

Given that the shedding frequencies of SIPeCS from the upstream rotors align with the surging frequencies of the downstream rotors ($\omega_S^{\text{up}} = \omega_S^{\text{down}}$), the arrival times of SIPeCS at the downstream rotor synchronize with the surging phase angle and surging velocity of the downstream rotor (ϕ_S^{down} and V_S^{down}). This synchronization makes variations in $\Delta_{\phi_{S_0}}$ affect $\overline{C}_P^{\text{down}}$, as the inflow conditions experienced by the downstream rotor are affected by the induction fields of the SIPeCS passing by. It is important to note that both V_S^{down} and the flow conditions around the downstream rotor profoundly influence C_P^{down}. Therefore, if the strengths of the SIPeCS shed by the upstream rotor are stronger upon reaching the downstream rotor, the performance of the downstream rotor will be more affected by the SIPeCS, making it more sensitive to the value of $\Delta_{\phi_{S_0}}$.

In Figs. 11(b) and 12(b), it is shown that values of $\langle \Gamma_u \rangle_{0\pi,\text{max}}$, which corresponds to the strength of the shear layer, collapse on to a same line for all the surging and fixed cases, confirming with what Li et al. [10] reported. This again highlights that $\langle \Gamma_w \rangle_{0\pi,\text{max}}$ is a more desired quantity for quantifying the strength of SIPeCS, as the contributions of $\langle \Gamma_u \rangle_{0\pi,\text{max}}$ to $\langle \Gamma \rangle_{0\pi,\text{max}}$ can be considered due to the background flows.

In Fig. 11(c), it can be seen that the values of $\langle \Gamma_w \rangle_{0\pi,\text{max}}$ for the surging cases (configuration SS) having $\Delta_D = 3D$ are significantly higher than those of the fixed case (configuration FF) right before the downstream rotor, showing that the influences of the SIPeCS shed by the upstream rotor remain. In the scenarios with $\Delta_D = 5D$, Fig. 12(c) shows that the values of $\langle \Gamma_w \rangle_{0\pi,\text{max}}$ for the surging cases have already dropped to a level very close to those of the fixed (reference) case, indicating that the SIPeCS shed by the upstream rotor are much more diluted by ambient turbulence before hitting the downstream rotor compared to the cases having $\Delta_D = 3D$. This is clearly reflected on the values of $\delta \overline{C}_P^{\text{down}}$ in Fig. 10, where $\delta \overline{C}_P^{\text{down}}$ for the cases having $\Delta_D = 3D$
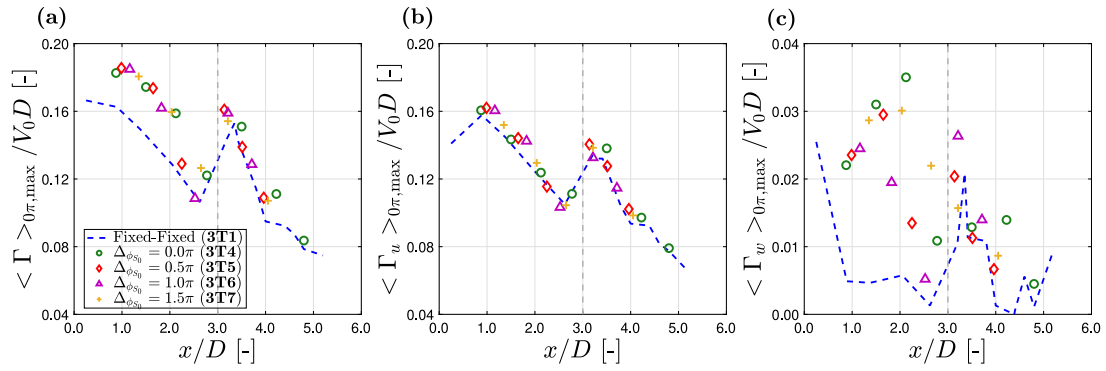
Fig. 11. $\langle\Gamma\rangle_{0\pi,\max}$ (local maxima of phase-averaged circulation), $\langle\Gamma_u\rangle_{0\pi,\max}$, and $\langle\Gamma_w\rangle_{0\pi,\max}$ against the x-positions where $\langle\Gamma\rangle_{0\pi,\max}$ are found for the cases with different $\Delta_{\phi_{S_0}}$ (phase difference of the two surging motions) and having $\Delta_D = 3D$ (labeled with a vertical dashed line). Case numbers are labeled in parentheses. $\langle\Gamma_u\rangle_{0\pi,\max}$ and $\langle\Gamma_w\rangle_{0\pi,\max}$ are calculated based on the same paths which $\langle\Gamma\rangle_{0\pi,\max}$ are obtained, but only considering $\langle u\rangle_{0\pi}$ or $\langle w\rangle_{0\pi}$ (definitions are in Eqs. (20) to (22)). (a): $\langle\Gamma\rangle_{0\pi,\max}$. (b): $\langle\Gamma_u\rangle_{0\pi,\max}$. (c): $\langle\Gamma_w\rangle_{0\pi,\max}$. Configuration FF here serves as a reference, and the vertical dashed line indicates the x-position of the downstream rotor. Values smaller than zero are omitted for clarity.
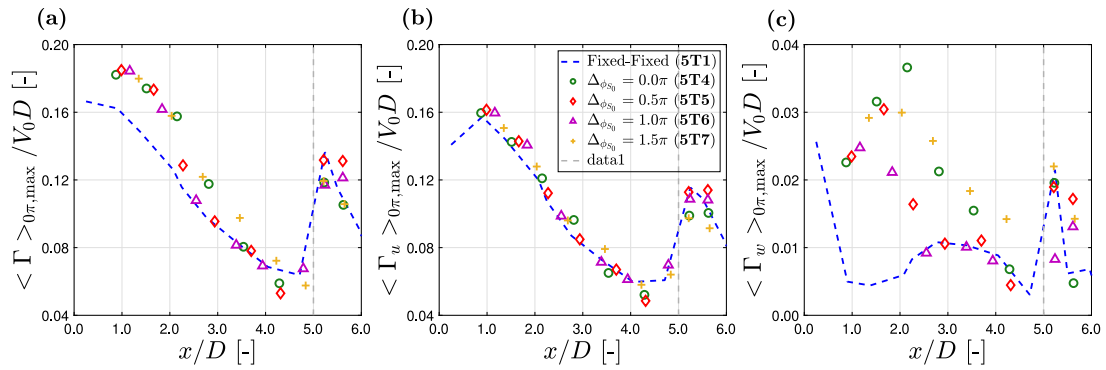

Fig. 12. Circulation plots as in Fig. 11 with larger rotor spacing of $\Delta_D = 5D$.

fluctuate more as varying $\Delta_{\phi_{S_0}}$ compared to those having $\Delta_D = 5D$. Additionally, this can also be observed with the contour plots of $\langle|\omega|\rangle_{0\pi}$ displayed in the bottom right of Fig. 7 (case **5T4**). It can be seen that the SIPeCS structures shed by the upstream rotor appear obviously until around $x/D = 3$, while they are practically indistinguishable at $x/D = 5$ by visual inspection.

Altogether, with the reported $\delta\overline{C}_P^{\,\text{up/down}}$ and the phase-averaged circulation-related quantities in this subsection, it can be concluded that $\Delta_{\phi_{S_0}}$ has limited effects on the cases having turbulent inflow, especially when Δ_D is larger ($\geq 5D$).

4. Conclusions

This work conducted a comprehensive large eddy simulation (LES) investigation of the wake interaction of two inline surging/fixed floating offshore wind turbine (FOWT) rotors by applying prescribed motions to the rotors. Two under-explored yet relevant aspects for FOWTs were examined, which are the different fixed–surging configurations and the phase differences between the surging motions of the two surging rotors ($\Delta_{\phi_{S_0}}$). Both aspects were tested with different inter-spacing between the two rotors ($\Delta_D = 3D/5D$) and different inflow conditions (laminar/turbulent, TI =5.3%), providing a thorough analysis and benchmark.

Analysis focusing on different fixed–surging configurations showed that when under laminar inflow conditions, the power output of the downstream rotor ($\overline{C}_P^{\,\text{down}}$) was significantly increased if the upstream rotor was surging compared to when it was fixed (~10% or ~40% when inter-spacing was $3D$ or $5D$). However, the increase fell to a mere ~1.5% when the inflow conditions had realistic turbulence intensity. In general, the power performances of the dual-rotor system benefited

from the considered surging motions compared to the fixed counterparts when under realistic turbulent inflow conditions (by up to around 2%, no controlling is involved for all cases). The power performance improvements were attributed to the surging motions and the enhanced wake recovery. For the former, given the identical conditions for the other parameters, results indicated that the power output of a rotor can be higher when it was surging compared to when it was fixed. Regarding the latter, fixing all other variables, the profiles of mean area-averaged streamwise velocity ($\overline{u}_{\text{Dsik}}$) were higher for cases with a surging upstream rotor than for those with a fixed upstream rotor. Note that higher $\overline{u}_{\text{Dsik}}$ in the wake naturally led to increased $\overline{C}_P^{\,\text{down}}$. Additionally, the contour plots and three-dimensional iso-surfaces also showed that the flow structures of the wake were dominated primarily by whether or not the upstream rotor was surging, where the effects of the surging configuration of the downstream rotor were much less pronounced.

Regarding the phase difference between the surging motions of the two rotors ($\Delta_{\phi_{S_0}}$), the simulation results showed that $\Delta_{\phi_{S_0}}$ has rather small impacts on power output of the dual rotor system when subjected to realistic turbulent inflow conditions (TI= 5.3%), especially when the inter-spacings between the two rotors were larger. The relative changes of $\overline{C}_P^{\,\text{down}}$ due to different $\Delta_{\phi_{S_0}}$ ($\delta\overline{C}_P^{\,\text{down}}$) were not greater than $\pm 1.0\%$ and $\pm 0.4\%$ when the inter-spacings were $3D$ and $5D$, respectively.

The findings of this study suggested that, as the inflow turbulence intensity matches the typical values for offshore environments, surging motions in FOWTs yielded modest improvements in overall power output. While these gains were relatively minor, they could potentially inform turbine layout and operational strategies for future floating offshore wind farms. Additionally, understanding the influences of fixed–surging configurations and phase differences of the motions, though turned out to be minor, provides nuanced insights into wake
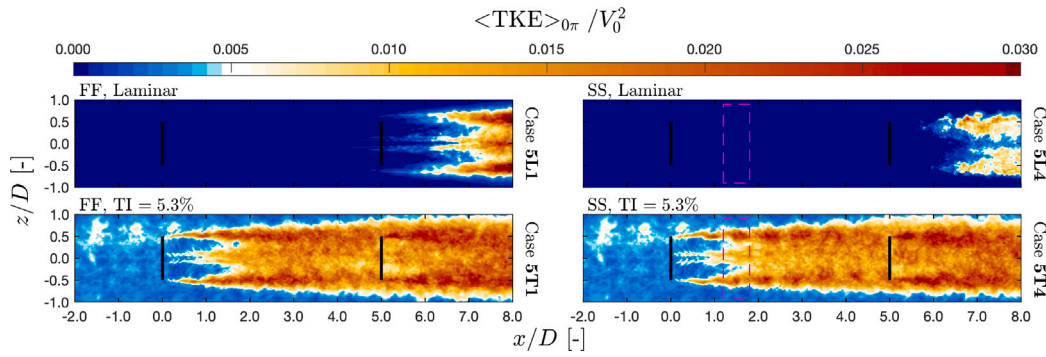
Fig. A.1. Contours of phase-averaged turbulent kinetic energy $< \text{TKE} >_{0\pi}$ of the selected cases with $\Delta_D = 5D$. Upper row: Cases with configuration FF and SS subjected to laminar inflow conditions. Lower row: Cases with configuration FF and SS subjected to turbulent inflow conditions (TI = 5.3%). The case numbers are labeled on the right of each panel. Example sets of SIPeCS identified in the SS cases are enclosed in boxes of dashed-line, and they have the same locations as those in Fig. 7.

interactions among FOWTs in motion. These insights may be useful in developing models aimed at predicting fatigue loading. Furthermore, if the observed limited impact of phase differences in surging motions can be extended to other types of FOWT motions, such as pitching and heaving, then phase differences of motions may potentially be excluded from consideration when designing and optimizing future floating offshore wind farms. However, further detailed investigations are recommended as part of future work.

CRediT authorship contribution statement

YuanTso Li: Writing – review & editing, Writing – original draft, Validation, Software, Methodology, Investigation, Formal analysis, Data curation, Conceptualization. **Wei Yu:** Writing – review & editing, Supervision, Project administration, Methodology, Formal analysis. **Hamid Sarlak:** Writing – review & editing, Supervision, Project administration, Methodology, Formal analysis, Conceptualization.

Declaration of competing interest

The authors declare that they have no known competing financial interests or personal relationships that could have appeared to influence the work reported in this paper.

Appendix A. Contours of phase averaged turbulent kinetic energy $< \text{TKE} >_{0\pi}$

The definition of (resolved) turbulent kinetic energy (TKE) and its relation to turbulence intensity (TI) used in this work are shown in Eq. (A.1). While TKE is commonly used as an indicator of flow's random fluctuations in wind energy applications [14], it presents a specific limitation for this study. That is, TKE includes periodic fluctuations, which are not truly stochastic. This is particularly relevant here, as the surging motions examined in this work are strictly periodic. To address this limitation, phase-averaged TKE ($<\text{TKE}>_{0\pi}$) is employed [10], as defined in Eq. (A.2), and definition of $\langle\sigma_u\rangle_{0\pi}$ is given in Eq. (A.3). Using $<\text{TKE}>_{0\pi}$, allows excluding fluctuations associated with the surging and rotor rotational periods (rotor rotational frequencies used in this work are designed based on the surging frequency, see Section 2.2), thereby enhancing the detection of truly stochastic signals. Note that

the notation here follows the phase-averaging operation described in Section 2.2.

$$\text{TKE} = \frac{1}{2}\left(\sigma_u^2 + \sigma_v^2 + \sigma_w^2\right), \qquad \text{TI} = \frac{\sqrt{\frac{2}{3}\,\text{TKE}}}{V_0} \qquad (A.1)$$

$$\langle\text{TKE}\rangle_{0\pi} \overset{\Delta}{=} \frac{1}{2}\left(\langle\sigma_u\rangle_{0\pi}^2 + \langle\sigma_v\rangle_{0\pi}^2 + \langle\sigma_w\rangle_{0\pi}^2\right) \qquad (A.2)$$

$$\langle\sigma_u\rangle_{0\pi} \overset{\Delta}{=} \sqrt{\frac{\Sigma_{n=1}^{N}\left(u_{0\pi,n} - \langle u\rangle_{0\pi}\right)^2}{N}} \qquad (A.3)$$

Phase-averaged TKE ($<\text{TKE}>_{0\pi}$) fields of the four most representative cases are presented in Fig. A.1. These cases are the same as those presented in Figs. 7 and 8. Focusing first on the two laminar cases in the top row, it can be seen that the $<\text{TKE}>_{0\pi}$ fields of two cases both have very low values, where significant values only appear $1D$ after the downstream rotor. Interestingly, the $<\text{TKE}>_{0\pi}$ field values for configuration SS (case **5L4**) are notably lower than those for configuration FF (case **5L1**), which contrasts with the TKE field trends shown in Fig. 8. This observation reaffirms the findings of Li et al. [10], which stated that when subjected to laminar inflow conditions, the wake of a harmonically surging rotor is more stable than that of a fixed rotor. This phenomenon appears to extend to a dual-rotor system in the present study. For the two turbulent cases in the bottom row, the $<\text{TKE}>_{0\pi}$ fields share a similar contour pattern (both the shape and magnitude) with the TKE fields presented in Fig. 8. However, configuration SS (case **5T4**) displays a feature absent in configuration FF (case **5T1**). That is, between the two rotors, bulbs of higher $<\text{TKE}>_{0\pi}$ values appear periodically along the streamwise direction. These structures, similar to those identified by Li et al. [10], are associated with SIPeCS, as they appear precisely at the locations where SIPeCS are detected. After the downstream rotor, bulbs of high $<\text{TKE}>_{0\pi}$ values become difficult to identify, again showing that the effects on wake structures for the surging downstream rotor are less significant compared to the upstream one.

Furthermore, Fig. A.1 can be directly compared to Figure 13 of the work of Li et al. [10] to assess the effects of the downstream rotor on the wakes. In general, the presence of the downstream rotor elevates the values of $<\text{TKE}>_{0\pi}$ field behind the downstream rotor, indicating that the randomness of the wake is increased and the breakdown of the wake is promoted.

Appendix B. Results regarding the phase differences of the surging motions between the two rotors at laminar inflow conditions

The relative differences of the time-averaged power outputs of the upstream/downstream rotors ($\delta\overline{C}_P^{\text{up/down}}$) for the laminar cases with SS configuration are overviewed in Fig. B.1. The definition of $\delta\overline{C}_P$ can be found in Eq. (19). As in the turbulent cases, the effects of $\Delta_{\phi_{S_0}}$ are
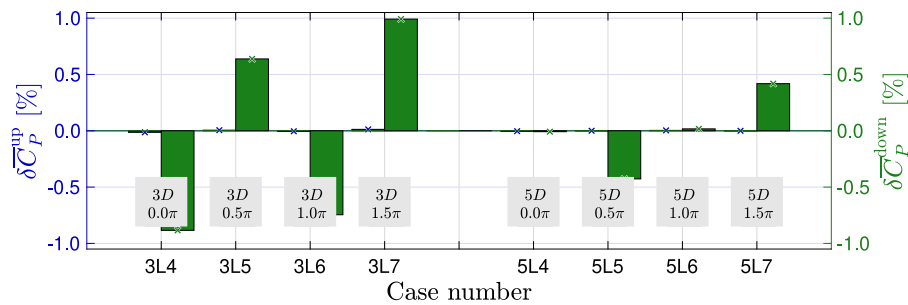
Fig. B.1. $\delta \overline{C}_P^{\,\mathrm{up}}$ and $\delta \overline{C}_P^{\,\mathrm{down}}$ for the SS cases with different $\Delta_{\phi_{S_0}}$ under laminar inflow conditions. The top entry stands for inter-spacing Δ_D and the bottom stands for the phase difference of the surging motions between the two rotors (in radians, denoted as $\Delta_{\phi_{S_0}}$ in the context). The averaged values for calculating $\delta \overline{C}_P$ of the four left/right cases are based on themselves.

generally mild on $\overline{C}_P^{\,\mathrm{down}}$ (but are stronger compared to turbulent cases), and the impacts decrease as Δ_D increases.

References

[1] G. van Kuik, J. Peinke, R. Nijssen, D. Lekou, J. Mann, J.N. Sørensen, C. Ferreira, J.-W. van Wingerden, D. Schlipf, P. Gebraad, et al., Long-term research challenges in wind energy–a research agenda by the European academy of wind energy, Wind Energy Sci. 1 (1) (2016) 1–39.

[2] P. Veers, K. Dykes, E. Lantz, S. Barth, C.L. Bottasso, O. Carlson, A. Clifton, J. Green, P. Green, H. Holttinen, et al., Grand challenges in the science of wind energy, Science 366 (6464) (2019) eaau2027.

[3] S. Butterfield, W. Musial, J. Jonkman, P. Sclavounos, Engineering Challenges for Floating Offshore Wind Turbines, Tech. Rep., National Renewable Energy Lab (NREL), Golden, CO (United States), 2007.

[4] D. Micallef, A. Rezaeiha, Floating offshore wind turbine aerodynamics: Trends and future challenges, Renew. Sustain. Energy Rev. 152 (2021) 111696.

[5] N. Ramos-García, S. González Horcas, A. Pegalajar-Jurado, S. Kontos, H. Bredmose, Investigation of the floating IEA wind 15-MW RWT using vortex methods part II: Wake impact on downstream turbines under turbulent inflow, Wind Energy 25 (8) (2022) 1434–1463.

[6] T.T. Tran, D.-H. Kim, A CFD study into the influence of unsteady aerodynamic interference on wind turbine surge motion, Renew. Energy 90 (2016) 204–228.

[7] H.M. Johlas, L.A. Martínez-Tossas, M.J. Churchfield, M.A. Lackner, D.P. Schmidt, Floating platform effects on power generation in spar and semisubmersible wind turbines, Wind Energy 24 (8) (2021) 901–916.

[8] R. Farrugia, T. Sant, D. Micallef, A study on the aerodynamics of a floating wind turbine rotor, Renew. Energy 86 (2016) 770–784.

[9] V.G. Kleine, L. Franceschini, B.S. Carmo, A. Hanifi, D.S. Henningson, The stability of wakes of floating wind turbines, Phys. Fluids 34 (7) (2022).

[10] Y. Li, W. Yu, H. Sarlak, Wake structures and performance of wind turbine rotor with harmonic surging motions under laminar and turbulent inflows, Wind Energy (2024) http://dx.doi.org/10.1002/we.2949.

[11] L. Vermeer, J.N. Sørensen, A. Crespo, Wind turbine wake aerodynamics, Prog. Aerosp. Sci. 39 (6–7) (2003) 467–510.

[12] J.F. Herbert-Acero, O. Probst, P.-E. Réthoré, G.C. Larsen, K.K. Castillo-Villar, A review of methodological approaches for the design and optimization of wind farms, Energies 7 (11) (2014) 6930–7016.

[13] H. Sarlak, C. Meneveau, J.N. Sørensen, Role of subgrid-scale modeling in large eddy simulation of wind turbine wake interactions, Renew. Energy 77 (2015) 386–399.

[14] R.J. Stevens, C. Meneveau, Flow structure and turbulence in wind farms, Annu. Rev. Fluid Mech. 49 (2017) 311–339.

[15] F. Porté-Agel, M. Bastankhah, S. Shamsoddin, Wind-turbine and wind-farm flows: a review, Bound.-Layer Meteorol. 174 (1) (2020) 1–59.

[16] A.S. Wise, E.E. Bachynski, Wake meandering effects on floating wind turbines, Wind Energy 23 (5) (2020) 1266–1285.

[17] A. Rezaeiha, D. Micallef, Wake interactions of two tandem floating offshore wind turbines: CFD analysis using actuator disc model, Renew. Energy 179 (2021) 859–876.

[18] S.-P. Breton, J. Sumner, J.N. Sørensen, K.S. Hansen, S. Sarmast, S. Ivanell, A survey of modelling methods for high-fidelity wind farm simulations using large eddy simulation, Phil. Trans. R. Soc. A 375 (2091) (2017) 20160097.

[19] S. Mancini, K. Boorsma, M. Caboni, M. Cormier, T. Lutz, P. Schito, A. Zasso, Characterization of the unsteady aerodynamic response of a floating offshore wind turbine to surge motion, Wind Energy Sci. 5 (4) (2020) 1713–1730.

[20] C. Bak, F. Zahle, R. Bitsche, T. Kim, A. Yde, L.C. Henriksen, M.H. Hansen, J.P.A.A. Blasques, M. Gaunaa, A. Natarajan, The DTU 10-MW reference wind turbine, in: Danish Wind Power Research 2013, 2013.

[21] J. Jonkman, S. Butterfield, W. Musial, G. Scott, Definition of a 5-MW Reference Wind Turbine for Offshore System Development, Tech. Rep., National Renewable Energy Lab.(NREL), Golden, CO (United States), 2009.

[22] P. Cheng, Y. Huang, D. Wan, A numerical model for fully coupled aerohydrodynamic analysis of floating offshore wind turbine, Ocean Eng. 173 (2019) 183–196.

[23] G.M. Stewart, A. Robertson, J. Jonkman, M.A. Lackner, The creation of a comprehensive metocean data set for offshore wind turbine simulations, Wind Energy 19 (6) (2016) 1151–1159.

[24] R. Kyle, Y.C. Lee, W.-G. Früh, Propeller and vortex ring state for floating offshore wind turbines during surge, Renew. Energy 155 (2020) 645–657.

[25] B. Wen, X. Tian, X. Dong, Z. Peng, W. Zhang, On the power coefficient overshoot of an offshore floating wind turbine in surge oscillations, Wind Energy 21 (11) (2018) 1076–1091.

[26] K.S. Hansen, R.J. Barthelmie, L.E. Jensen, A. Sommer, The impact of turbulence intensity and atmospheric stability on power deficits due to wind turbine wakes at horns rev wind farm, Wind Energy 15 (1) (2012) 183–196.

[27] Y. Li, Numerical Investigation of Floating Wind Turbine Wake Interactions Using LES-AL Technique (Master's thesis), Technical University of Denmark/Delft University of Technology, Lyngby, Denmark/Delft, The Netherlands, 2023.

[28] DTU Computing Center, DTU computing center resources, 2022, http://dx.doi.org/10.48714/DTU.HPC.0001.

[29] R. Poletto, T. Craft, A. Revell, A new divergence free synthetic eddy method for the reproduction of inlet flow conditions for LES, Flow Turbul. Combust. 91 (2013) 519–539.

[30] P. Bachant, A. Goude, D. mec Martin Wosnik, Turbinesfoam: v0.1.1, 2019, http://dx.doi.org/10.5281/zenodo.3542301.

[31] J.N. Sorensen, W.Z. Shen, Numerical modeling of wind turbine wakes, J. Fluids Eng. 124 (2) (2002) 393–399.

[32] N. Troldborg, Actuator line modeling of wind turbine wakes, 2009.

[33] K.O. Dağ, J.N. Sørensen, A new tip correction for actuator line computations, Wind Energy 23 (2) (2020) 148–160.

[34] S.F. Hoerner, Fluid-Dynamic Drag: Theoretical, Experimental and Statistical Information, Copyright by: SF Hoerner Fluid Dynamics, Printed in the USA, Card Number 64-19666, 1965.

[35] S. Naderi, F. Torabi, Numerical investigation of wake behind a HAWT using modified actuator disc method, Energy Convers. Manage. 148 (2017) 1346–1357.

[36] Y. Li, W. Yu, H. Sarlak, Supplementary benchmark data and case settings for "wake interaction of dual surging FOWT rotors in tandem", 2024, http://dx.doi.org/10.4121/07267e2b-58a2-4600-9821-2b6648cb423a, (DOI reserved) URL https://data.4tu.nl/private_datasets/F88ybXTK37u7b-_S5ASKhE_aR1O3liXIDd_UsUMcZJM.

[37] D. Medici, S. Ivanell, J.-A. Dahlberg, P.H. Alfredsson, The upstream flow of a wind turbine: blockage effect, Wind Energy 14 (5) (2011) 691–697.

[38] Y. Li, W. Yu, H. Sarlak, Rotor performance and wake interaction of controlled dual surging fowt rotors in tandem, in: Journal of Physics: Conference Series, Vol. 2767, IOP Publishing, 2024, 092041, http://dx.doi.org/10.1088/1742-6596/2767/9/092041.

[39] J.F. Manwell, J.G. McGowan, A.L. Rogers, Wind Energy Explained: Theory, Design and Application, John Wiley & Sons, 2010.

[40] H. Sarlak, Large Eddy Simulation of Turbulent Flows in Wind Energy, (PhD thesis), Technical University of Denmark, Lyngby, Denmark, 2014.

[41] P.-A. Krogstad, P.E. Eriksen, "Blind test" calculations of the performance and wake development for a model wind turbine, Renew. Energy 50 (2013) 325–333.

[42] H. Johlas, L.A. Martínez-Tossas, D. Schmidt, M. Lackner, M.J. Churchfield, Large eddy simulations of floating offshore wind turbine wakes with coupled platform motion, in: Journal of Physics: Conference Series, Vol. 1256, IOP Publishing, 2019, 012018.

[43] K.M. Kopperstad, R. Kumar, K. Shoele, Aerodynamic characterization of barge and spar type floating offshore wind turbines at different sea states, Wind Energy 23 (11) (2020) 2087–2112.